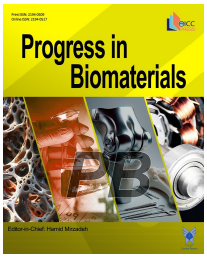

Volume 14, Issue 1, 142503 (1-20)

Progress in Biomaterials (PIBM)

https://doi.org/10.57647/pibm-2025-17505

Angiogenesis and *In Vitro* Bone Differentiation of HMSCs on PCL Nanofiber Scaffolds Containing Homogenized Platelet-Rich Fibrin-Chitosan Nanoparticles: An *In ovo* CAM Model

Mansoor Alizadeh[1], Mahboobeh Mahmoodi[1,2,*]

[1]*Department of Biomedical Engineering, Ya. C., Islamic Azad University, Yazd, Iran.*
[2]*Joint Reconstruction Research Center, Tehran University of Medical Sciences, Tehran, Iran.*

[*]**Corresponding author:** ma.mahmoodi@iau.ac.ir

Original Research

Received:
1 February 2025
Revised:
25 March 2025
Accepted:
30 March 2025
Published in issue:
31 March 2025

Abstract:

Bone regeneration remains a major clinical challenge, as current scaffolds rarely replicate the optimal microenvironment required for effective tissue repair, particularly in stimulating vascularization. This study aimed to develop and evaluate a polycaprolactone (PCL) nanofiber scaffold incorporating chitosan (CH) nanoparticles loaded with homogenized platelet-rich fibrin (PCL/CH-hPRF) for bone tissue engineering. Scaffolds were fabricated via electrospinning and characterized by dynamic contact angle measurements, mechanical testing, degradation test, and *in vitro* bioactivity. Also, biological performance was evaluated by protein adsorption, MG-63 cell biocompatibility, and osteogenic differentiation of human mesenchymal stem cells (HMSCs) through alkaline phosphatase activity, calcium deposition, and Alizarin red staining. Furthermore, angiogenic potential was investigated using the *in ovo* chorioallantoic membrane (CAM) assay. Incorporating CH-hPRF nanoparticles into PCL nanofibers reduced the average fiber diameter from 230 nm in PCL scaffolds to 189 nm in PCL/CH-hPRF scaffolds. The PCL/CH-hPRF scaffold showed an increased degradation rate relative to other scaffolds, which can be attributed to enhanced fluid infiltration driven by its increased porosity and lower contact angle. The PCL/CH-hPRF scaffolds exhibited a significantly higher elastic modulus (45.35 MPa) compared to PCL scaffolds (35.53 MPa). Moreover, the hPRF release from the PCL/CH-hPRF scaffold reachesd 31.25% after 14 days, indicating a gradual and prolonged release of hPRF from the nanofibrous scaffold. After 28 days of immersion in simulated body fluid (SBF), the PCL/CH-hPRF scaffold exhibited higher bioactivity and enhanced biomineralization compared to the PCL scaffold. The PCL/CH-hPRF scaffold demonstrated excellent cell compatibility and promoted rapid osteogenic differentiation of HMSCs, with substantial calcium deposition observed over 14 days. Furthermore, the *in ovo* CAM assay revealed that the PCL/CH-hPRF scaffold induced approximately threefold higher blood vessel formation compared to the CH-hPRF scaffold. These results suggest that the PCL/CH-hPRF composite nanofiber scaffold possesses superior osteogenic, angiogenic, and biological properties, making it a promising candidate for bone tissue engineering applications.

Keywords: *In ovo* CAM; Osteogenic differentiation; Homogenized platelet-rich fibrin; Biomineralization; Electrospinning; Nanofiber scaffold

Cite this article: Alizadeh, M., Mahmoodi, M. Angiogenesis and *In Vitro* Bone Differentiation of HMSCs on PCL Nanofiber Scaffolds Containing Homogenized Platelet-Rich Fibrin-Chitosan Nanoparticles: An *In ovo* CAM Model. *Progress in Biomaterials* **14**(1), Article 03 (2025).

1. Introduction

Bone is the main mechanical support system in the human body, which is constantly changing and self-healing. Although small bone lesions are regenerated by spontaneous processes, large lesions cannot be repaired without medical interventions due to several reasons such as misplaced bone

fusion, complete loss of bone due to injury, and infection of the lesion site. The use of autograft, allograft, xenograft, and bone tissue engineering scaffolds are among the medical interventions in the repair of bone [1, 2] lesions. Nowadays, the grafts are challenging due to the limitations of their use such as immune reactions, tissue infection, lack of donors, and chronic pain [3]. Bone tissue engineering reconstructs and repairs damaged tissue by providing the possibility of regrowth of tissue in a natural way. The design of a bone scaffold requires a proper physical structure that allows cell proliferation and cell adhesion. Bone tissue engineering has been developed with suitable materials for making scaffolds, growth factors, and stem cells to reduce or eliminate the adverse effects resulting from common methods of treating bone lesions, increase interactions with adjacent tissues, and stimulate bone formation [4]. Furthermore, the three-dimensional (3D) structure of the scaffold is a significant agent in the process of tissue repair and ultimately determining the fate of stem cells [5, 6]. Human mesenchymal stem cells (HMSCs) can differentiate into multiple cell types that play an important role in regenerative medicine. HMSCs are also used in tissue engineering studies because they are easily extracted from the bone marrow and multiplied easily in culture conditions [7].

Researchers have studied several methods such as electrospinning [8], freeze-drying [9], freeze-casting [10], solvent casting [11], phase separation [12], and 3D printing [13] to make bone scaffolds. However, these methods have various advantages and disadvantages that limit their use. The electrospinning method is among the most common methods for making bone tissue scaffolds. The process of making a scaffold with the electrospinning method is straightforward and cheap and due to the remarkable similarity of electrospun fibers to the structure of the natural extracellular matrix (ECM), this technique has garnered significant interest among researchers as a promising approach for restoring the function of damaged tissues [4, 14, 15]. In recent years, the use of biodegradable polymers has significantly increased in various biomedical fields such as medicine, pharmaceuticals, drug delivery systems, and tissue engineering. Among them, synthetic aliphatic polyesters stand out due to their favorable biodegradability and biocompatibility characteristics. Their advantage lies in their safe interaction with living tissues and their effective degradation under physiological conditions. Polycaprolactone (PCL) is a biocompatible polyester material approved by the US Food and Drug Administration (FDA) for use in hard and soft tissues [16]. PCL is a low-cost biopolymer with excellent mechanical properties, biodegradability, and non-toxicity with slow degradation. One of the main reasons for its widespread use in fabricating tissue engineering scaffolds via electrospinning is its excellent biocompatibility with other biopolymers. Its favorable processability allows for the formation of diverse shapes and structures, and its high thermal stability makes it easy to melt and handle. Thus, PCL is extensively utilized in scaffold fabrication due to its biocompatibility, biodegradability, and moldability. Although PCL exhibits excellent physical, chemical, biological, and mechanical characteristics, it lacks the reactive functional groups required to enhance specific cellular activities like cell adhesion. To overcome this limitation, researchers often blend PCL with natural polymers like chitosan (CH) or incorporate ceramic nanoparticles to enhance its bioactivity [17–19]. Chitosan (CH) is a natural, hydrophilic polysaccharide obtained through the alkaline deacetylation of chitin It is widely used in biomedical applications due to its favorable properties, including high biocompatibility, biodegradability, hemostatic activity, wound healing potential, and antimicrobial activity. In recent years, increasing attention has been paid to CH-based composite materials for bone tissue engineering, as CH promotes ECM growth and formation, leading to appropriate cellular responses [20]. CH stimulates the secretion of interleukin-1 (IL-1) and growth factors, which enhance cell proliferation and activity on scaffold surfaces. Additionally, the presence of glucosamine in CH induces cytokine production, increases macrophage secretion, stimulates tissue regeneration, and helps prevent infection at the injury site. These combined effects promote cell growth and proliferation. The antioxidant ability of CH reduces active species of oxidative stress (ROS), which ultimately induces the production and increases the release of growth factors and cell differentiation. As a hydrophilic material with a positively charged surface, CH also improves cell adhesion, proliferation, and differentiation when incorporated into composite scaffolds [21].

Platelet-rich fibrin (PRF) is a natural fibrin network enriched with platelets and multiple bioactive factors, forming a complex three-dimensional structure. It contains key growth factors, including transforming growth factor-beta 1 (TGF-β1), platelet-derived growth factor (PDGF), vascular endothelial growth factor (VEGF), as well as glycoproteins like thrombospondin-1. This dense mesh of fibrin, cytokines, and structural proteins supports and accelerates processes involved in wound healing and tissue regeneration [22, 23]. PRF gradually releases significant amounts of growth factors such as PDGF, insulin-like growth factor-1 (IGF-1), TGF-β1, and VEGF, which together promote rapid bone repair and stimulate new blood vessel formation and angiogenesis [24]. Among the notable benefits of PRF in bone healing are its biocompatibility, ability to speed up tissue regeneration, and its straightforward, cost-effective preparation without complex processing steps. Despite these advantages, using PRF alone has limitations due to its short shelf life and sensitivity to storage conditions. To overcome these challenges, incorporating PRF into carrier materials or encapsulating it can provide a sustained and controlled release of its growth factors, enhancing its effectiveness in regenerative applications [25].

Semnani et al. [19] developed and characterized electrospun scaffolds composed of PCL and CH. The resulting fibers indicated an average diameter of 243 nm, with a porosity of 79% and pore sizes around 5 μm. These PCL/CH nanofiber scaffolds supported robust adhesion, growth, and proliferation of rat liver epithelial cells. Ye et al. [26] produced electrospun PCL/CH membranes integrated with calcium phosphate doped with strontium, resulting in a structure that closely mimics the ECM while exhibiting

promising biological and mechanical properties suitable for bone tissue engineering. These nanofiber constructs demonstrated strong bioactivity, promoted bone formation and osteogenesis, and supported angiogenesis. Surucu et al. [27] fabricated core-shell nanofiber scaffolds of PCL and CH using electrospinning for tissue engineering applications. Their findings highlighted that combining PCL and CH not only optimized the electrospinning process but also enhanced fibroblast cell proliferation. Additionally, Shimojo et al. [28] prepared composite scaffolds of CH and PRF via freeze-drying, achieving controlled release of growth factors. They reported significant improvements in stem cell proliferation and differentiation on these scaffolds. Chi et al. [29] designed composite scaffolds combining CH, gelatin, and PRF, which exhibited desirable mechanical strength, appropriate porosity levels, and favorable pore sizes. These scaffolds effectively supported cell adhesion, proliferation, and osteogenic differentiation, indicating their potential for bone tissue regeneration. In another research [30], collagen/CH/PRF composite membrane was prepared by freeze-drying method for dental applications. Incorporating PRF into these membranes reduced degradation rates, increased elastic modulus, improved cell viability, and enhanced osteogenic differentiation, making them promising candidates for oral tissue repair.

Despite the development of numerous scaffolds for bone tissue engineering, none have successfully recreated the optimal microenvironment required for effective bone regeneration, particularly in promoting vascularization. In this study, we designed and fabricated a novel electrospun nanofiber scaffold composed of PCL integrated with CH-hPRF nanoparticles. This composite electrospun nanofiber scaffold uniquely combines the mechanical support and stability of PCL fibers with the biological activity of CH-hPRF nanoparticles and CH. The CH-hPRF nanoparticles provid a sustained release of hPRF from the scaffold that enhances osteogenic differentiation and angiogenesis, while the CH component contributes biocompatibility and favorable cell-interactive features. The primary objective of this research was to investigate how incorporating CH-hPRF nanoparticles into PCL nanofibers affected the mechanical, biological, osteogenic, and angiogenic properties of the scaffold. Our central hypothesis was that adding CH-hPRF nanoparticles to PCL-based scaffolds would significantly enhance protein adsorption, bioactivity, biomineralization, osteogenic differentiation of HMSCs, and angiogenesis. The innovation of this study lies in developing a multifunctional scaffold that enhances biomechanical strength and biological performance through synergistic promotion of osteogenesis and angiogenesis. In addition, the *in ovo* chicken chorioallantoic membrane (CAM) assay was employed as a cost-effective, animal-sparing method to evaluate the scaffold's angiogenic potential, offering a promising solution for bone defect repair in clinical applications.

2. Materials and methods

2.1 Materials

In this study, polycaprolactone (PCL, Mw: $70-90$ kDa), medium molecular weight chitosan (98% purity, 85% degree of deacetylation), and sodium tripolyphosphate (TPP) were procured from Sigma-Aldrich. The chemicals, including ethanol, isopropanol, acetic acid (1 M), and formic acid (1 M) were sourced from Merck. L-ascorbic acid 2-phosphate, β-glycerolphosphate, glutaraldehyde, Roswell Park Memorial Institute medium (RPMI), phosphate-buffered saline (PBS), and 3-(4,5-dimethylthiazol-2-yl)-2,5-diphenyltetrazolium bromide (MTT) were provided by Sigma-Aldrich. Fetal bovine serum (FBS), simulated body fluid (SBF), and Dulbecco's Modified Eagle Medium/F12 (DMEM/F12) were purchased from Gibco.

2.2 Preparation of hPRF and CH-hPRF nanoparticles

PRF was prepared using the Choukroun method [31]. Briefly, human blood was first collected in a glass tube without anticoagulant and immediately centrifuged at 2700 rpm for 12 min. After centrifugation, the supernatant layer was discarded, and the remaining fibrin gel was carefully extracted from the tube, separating it from the sedimented red blood cell layer. The PRF was then transferred using sterile forceps and homogenized with SBF using a homogenizer at 800 rpm for 10 min, yielding a uniform PRF suspension (hPRF).

To prepare CH-hPRF nanoparticles, 30 mg of CH was dissolved in 25 mL of a 1% aqueous acetic acid solution, resulting in a suspension of CH nanoparticle suspension. The homogenized PRF solution was then added to the CH suspension, and the mixture was homogenized at 800 rpm for 2 hr. Next, 25 mg of TPP solution was gradually introduced into the CH-hPRF mixture, which was subsequently homogenized for an additional 30 min. The resulting suspension was centrifuged at 2000 rpm for 20 min. Finally, the collected CH-hPRF nanoparticles were frozen and lyophilized using a freeze dryer (ScanVac CoolSafe, ScanLaf, Denmark) at -80 °C for 48 hr. The steps involved in CH-hPRF preparation and the chemical formula of hPRF are illustrated in Fig. 1 (a-b).

2.3 Preparation of nanofiber scaffold

CH containing hPRF at a concentration of 2% and CH alone at 2% were each dissolved separately in an acetic acid/formic acid solvent mixture (3:1) using a magnetic stirrer. PCL was dissolved at a concentration of 15% in the same solvent mixture and stirred for 24 hr. Each CH solution, with and without hPRF, was separately mixed with the PCL solution at a 3:2 ratio, and the mixtures were stirred for 20 min. As a result, PCL, PCL/CH, and PCL/CH-hPRF solutions were prepared. Electrospun nanofiber scaffolds of PCL, PCL/CH, and PCL/CH-hPRF were manufactured using an electrospinning apparatus (KYKY-2200). The electrospinning process parameters, including applied voltage, feeding rate, and needle-to-collector distance, were optimized based on protocols reported in the literature to achieve uniform nanofiber morphology and desired scaffold properties [32, 33]. The prepared solutions were loaded into syringes equipped with needles of 0.6 mm diameter and 4 cm length. Electrospinning of PCL and PCL/CH scaffolds was performed with a feeding rate of 0.1 mL/hr, a needle-to-collector distance of 12 cm, and an applied voltage of 19 kV. For the PCL/CH-hPRF scaffold, electrospinning was con-

ducted with a feeding rate of 0.3 mL/hr, a distance of 15 cm, and a voltage of 22 kV. Figure 1 (b) presents a schematic illustration of the scaffold fabrication process via electrospinning and the chemical structures of biomaterials and their interactions through hydrogen bonding.

2.4 Characterization of the nanofiber scaffolds

2.4.1 Morphology and structure of scaffolds

A scanning electron microscope (KYKY EM3200-SEM) was used to examine the morphology and diameter of the electrospun fibers. Prior to imaging, the samples were coated with a thin layer of gold. Imaging was performed at an accelerating voltage set to 30 kV. The diameters of numerous randomly selected nanofibers were determined using MIP software, and the average fiber diameter was calculated.

2.4.2 Porosity of scaffolds

The liquid displacement method was used to measure the porosity percentage of the scaffolds. In this method, the scaffold was immersed in a graduated cylinder containing ethanol with an initial volume of v_1 and kept for 5 min to ensure complete saturation. The total volume after immersion, including the scaffold and ethanol, was recorded as v_2. After removing the scaffold, the remaining volume of ethanol in the cylinder was measured as v_3. The pore volume was calculated using the equation $(v_1 - v_3)$. Finally, the average porosity percentage of the scaffold was determined using equation (1) [34].

$$\text{Porosity}(\%) = \frac{v_1 - v_3}{v_2 - v_3} \times 100 \tag{1}$$

2.4.3 Fourier transform infrared spectroscopy

The identification of functional groups and chemical bonds in the scaffolds was performed using Fourier transform infrared (FTIR) spectroscopy (BRUKER TENSOR 27, Germany). For this analysis, the samples were finely ground, mixed with potassium bromide (KBr), and pressed into thin pellets. Infrared (IR) absorption spectra were recorded over the wavenumber range of $400 - 4000\ \text{cm}^{-1}$. The types of chemical bonds were determined by analyzing the absorption bands observed in the FTIR spectra.

2.4.4 Surface wettability

In this study, the hydrophilicity of the nanofiber surfaces was measured using a dynamic contact angle method with a contact angle analyzer to minimize error and improve measurement accuracy given the hysteresis of nanofiber surfaces. The dynamic measurement was based on the Wilhelmy plate method, which allows determining the contact angle between a solid surface and a liquid with a known surface tension. Distilled water (DI), with a surface tension of 72 dyn/cm, was used as the test liquid to assess the hydrophilic or hydrophobic properties of the scaffolds. For

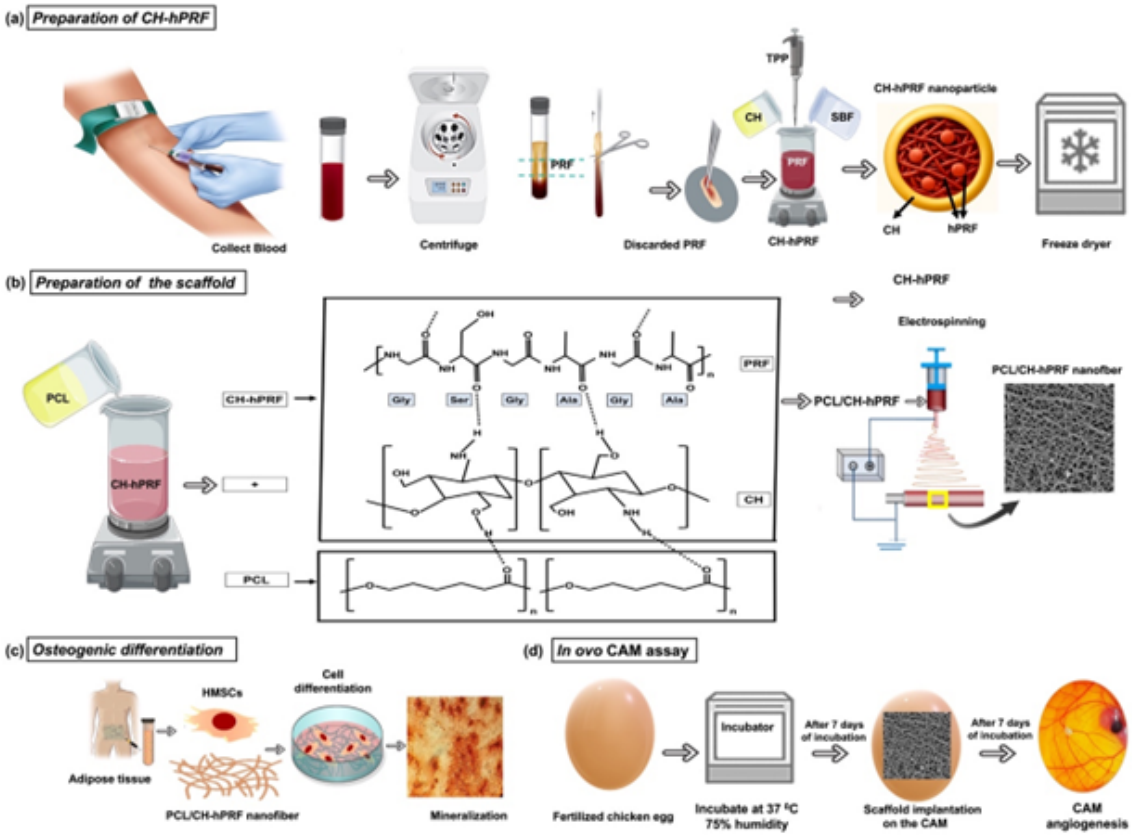

Figure 1. Schematic illustration of (a) CH-hPRF preparation; (b) Fabrication of the PCL/CH-hPRF scaffold using the electrospinning method and the chemical structures of PCL, chitosan, hPRF and their interactions through hydrogen bonding, the amino acids present in hPRF include Glycine (Gly), Serine (Ser), and Alanine (Ala); (c) Stages of differentiation of human mesenchymal stem cells into osteoblasts; and (d) *In ovo* angiogenic assay in chick embryo.

the experiment, nanofibers were electrospun onto both sides of glass coverslips measuring 2 cm in width. During testing, the stage holding the liquid reservoir moved upward at a speed of 1 mm/s until the scaffold was submerged, after which the speed was reduced to 0.2 mm/s. The stage then moved downward to complete a reciprocating motion, while changes in the sample's weight were recorded to generate a force-displacement curve. The water contact angle (θ) was calculated using equation (2).

$$\sigma \cos\theta = \frac{\Delta w}{\rho} \tag{2}$$

where σ is the surface tension of liquid, θ is the water contact angle, Δw is the change in weight, and ρ is the wetted perimeter of the sample. The contact angle was determined in reciprocating mode using SCAT software through graph analysis, and the average contact angle was reported.

2.4.5 Degradation assay

The nanofibrous scaffolds were electrospun onto glass coverslips with a diameter of 15 mm, following the ASTM F1635 standard for biodegradability assessment. After fabrication, the samples were carefully separated from the coverslips, and their initial weight (W_0) was measured using a digital scale. Subsequently, the samples were immersed in PBS and incubated at 37 °C. At predetermined time points (1, 2, 3, 4, 5, and 6 weeks), the samples were retrieved, rinsed twice with DI water, dried, and weighed again (W_t). The degradability percentage was then calculated using equation (3) [17].

$$\text{Weight loss}(\%) = \frac{W_0 - W_t}{W_0} \times 100 \tag{3}$$

FESEM scanning electron microscope (Quanta 450 FEG) was used to evaluate surface morphological changes induced by degradation. Scaffold surfaces after 5 and 6 weeks of PBS incubation were imaged to observe structural alterations.

2.4.6 Mechanical test

The mechanical strength and elastic modulus of the scaffolds were evaluated using a universal testing machine (Zwick/Roell Universal Testing Machine-Model $1446-60$). In accordance with the ASTM D882 standard, 3 mL of each polymer solution was electrospun to fabricate the scaffolds. The thickness of the nanofiber scaffolds was measured using a precision thickness gauge with an accuracy of 0.01 mm, and was approximately $100-200$ µm. The scaffolds were then cut into rectangular specimens measuring $60 \times 10 \times 2$ mm along the longitudinal direction and mounted on a paper mold for mechanical testing. Tensile testing was conducted under controlled environmental conditions with an applied load of 10 N, a crosshead speed of 10 mm/min, 30% relative humidity, and a temperature of 25 °C.

2.4.7 Release kinetics of hPRF

The quantification of hPRF release from CH-hPRF nanoparticles and PCL/CH-hPRF scaffolds was performed using a bicinchoninic acid (BCA) protein assay kit (Pierce^{TM}, Rockford Thermo Fisher Scientific), following the manufacturer's protocol. In this experiment, 16 µg/µL of free hPRF and 16 µg/µL of PCL/CH-hPRF sample were each placed in 30 mL of PBS with pH 7.4 and maintained in a shaking incubator at 37 °C with an agitation rate of 100 rpm for 14 days. At predetermined time intervals (5 h, 10 h, 15 h, days $1-14$), 0.5 mL of the release medium was withdrawn and immediately replenished with an equal volume of fresh PBS. The collected release medium was reacted with the BCA reagent, resulting in the formation of a purple complex. The intensity of this color is directly related to the concentration of hPRF present. The absorbance of this complex was then recorded at 562 nm using a spectrophotometer and cumulative release profiles were plotted. Encapsulation efficiency (EE) for CH-hPRF nanoparticles was determined using equation (4) [35].

$$\text{EE}(\%) = \frac{\text{Total concentration of hPRF} - \text{Concentration of free hPRF}}{\text{Total concentration of hPRF}} \times 100 \tag{4}$$

To gain insight into the underlying mechanisms governing hPRF release from CH-hPRF and PCL/CH-hPRF scaffolds, the release data were analyzed using the Higuchi and Ritger-Peppas mathematical models [36, 37]. The Higuchi model, derived from Fick's law of diffusion, establishes a linear correlation between the cumulative amount of hPRF released and the square root of time (equation (5)). In this formulation, "X" represents the cumulative drug release at a given time "t", while "K_H" denotes the Higuchi release constant, characterizing the diffusion rate through the samples.

$$K_H = \frac{X}{\sqrt{t_X}} \tag{5}$$

The Ritger-Peppas model describes drug release as a power-law relationship between the fraction of released drug and time (equation (6)). Here, M_t and M_∞ represent the drug amount released at time t and the total amount initially loaded, respectively, while K is a kinetic constant and n is the release exponent associated with the prevailing release mechanism. Values of $n \leq 0.43$ suggest a Fickian diffusion-dominated process, $0.43 < n < 0.8$ indicate non-Fickian transport, involving both diffusion and matrix relaxation, and $n \geq 0.8$ correspond to zero-order kinetics with a constant release rate. It is worth noting that the predictive accuracy of these kinetic models is generally confined to the initial phase of release, typically up to 60% of the total drug liberated, beyond which changes in matrix structure and other factors may cause deviations from the idealized model behavior.

$$\frac{M_t}{M_\infty} = K.t^n \tag{6}$$

2.4.8 Bioactivity test

The samples were immersed in SBF solution for 28 days and incubated at 37 °C to evaluate the bioactivity of PCL, PCL/CH, and PCL/CH-hPRF nanofiber scaffolds. The SBF was prepared according to the method developed by Kokubo et al. [38], ensuring ion concentrations similar to those found in human blood plasma. After 28 days of immersion, the scaffolds were removed, rinsed twice with DI water, and

air-dried. FESEM (Quanta 450 FEG) was used to observe the scaffold surfaces and assess the formation of apatite-like precipitates. Elemental analysis of the SBF solution was performed on days 7, 14, 21, and 28 using inductively coupled plasma optical emission spectrometry (ICP-OES, Optima 7300 DV, PerkinElmer, Shelton, USA) to quantify calcium ion concentration and evaluate the calcium depletion rate over time.

2.5 *In vitro* studies

2.5.1 MTT assay

Cell viability on the scaffold surfaces was assessed using the MTT assay. The scaffolds were fabricated by electrospinning directly onto glass coverslips, followed by sterilization through gamma irradiation. A direct contact approach was employed to evaluate potential cytotoxicity and cell proliferation. MG-63 osteoblast-like cells (NCBI C555) were sourced from the Pasteur Institute of Iran's cell bank. Following thawing, the cells were cultured in RPMI medium supplemented with 10% FBS and incubated at 37 °C under 90% humidity and 5% CO_2. The culture medium was refreshed every three days. For the MTT test, scaffolds were placed in the wells of a 12-well culture plate. Each scaffold received 1×10^4 MG-63 cells dispersed in 10 µL of medium, followed by incubation at 37 °C for 4 hr to allow cell attachment. Control wells ($n = 3$) containing culture medium without scaffolds were also included. After 72 hr, the culture medium was removed and replaced with 500 µL of MTT solution (0.5 mg/mL), followed by 4 hr of incubation. Then, the MTT solution was discarded, followed by the addition of isopropanol to solubilize the formazan crystals produced by metabolically active cells. The plate was gently shaken for 15 min to ensure complete dissolution. The resulting solution was transferred to a 96-well plate, and absorbance was measured at 570 nm using a microplate reader (STAT FAX 2100, USA). Higher optical density (OD) readings indicated greater cell proliferation on the scaffolds. Cell viability (%) was calculated using the equation (7).

$$\text{Cell viability}(\%) = \frac{\text{OD}_{\text{Sample}}}{\text{OD}_{\text{Control}}} \times 100 \qquad (7)$$

2.5.2 Cell adhesion

To evaluate cell adhesion on the scaffold surfaces, sterilized scaffolds were placed individually into the wells of a 24-well culture plate. Subsequently, 2×14 cells suspended in 100 µL of medium were seeded onto each scaffold and incubated for 4 hr to allow initial cell attachment. After this period, 1 mL of culture medium supplemented with 10% FBS was added to each well. Following 24 hr of incubation, the medium was removed and the scaffolds were rinsed with PBS to eliminate non-adherent cells. To fix the adhered cells, a 2.5% (w/v) glutaraldehyde solution was added to each well, and the samples were stored at 4 °C for 2 hr. The fixative was then discarded, and the scaffolds were sequentially dehydrated using DI water followed by graded ethanol series (50%, 60%, 70%, 80%, and 96%). Finally, the morphology and attachment of cells on the scaffold surfaces were examined using SEM.

2.5.3 Protein absorption

To assess protein adsorption by the PCL, PCL/CH, and PCL/CH-hPRF scaffolds, FBS was used as a model protein. Coverslips containing nanofibers were mounted in the wells of a 24-well culture plate, sterilized with 75% ethanol for 2 hr, and subsequently rinsed and soaked in PBS for 2 hr. Each sample was then incubated with 1 mL of 10% FBS at 37 °C for 24 hr. The amount of protein adsorbed was determined by measuring the absorbance of the FBS solution at 280 nm, both before and after incubation. Quantification was performed using a standard calibration curve generated with known concentrations of FBS [39, 40].

3. Cell differentiation

In this study, human mesenchymal stem cells (HMSCs) derived from human adipose tissue were obtained from the cell bank of the Pasteur Institute of Iran. The cells were initially cultured in DMEM/F12 medium supplemented with 10% FBS and incubated under standard conditions (37 °C, 90% humidity, and 5% CO_2). The culture medium was refreshed every three days to support optimal cell growth. To assess osteogenic differentiation, three assays were employed: alkaline phosphatase activity, Alizarin red staining, and calcium deposition analysis. In each test, wells containing cells cultured in osteogenic differentiation medium without scaffolds were used as controls. The overall procedure for evaluating stem cell differentiation into osteoblasts is illustrated in Fig. 1 (c).

3.0.1 ALP activity

To assess alkaline phosphatase (ALP) activity, HMSCs were enzymatically detached using trypsin after reaching the desired confluency. A total of 5000 cells suspended in 300 µL of culture medium containing 10% FBS were seeded onto each gamma-sterilized scaffold. The scaffolds were placed in the wells of a culture plate, and incubated at 37 °C with 90% humidity and 5% CO_2. After 24 hr, once cell adhesion to the scaffolds was confirmed, 1 mL of osteogenic differentiation medium was added to each well. This medium consisted of DMEM/F12 supplemented with 10% FBS, 1 mM dexamethasone, 50 µg/mL L-ascorbic acid 2-phosphate, and 10 mM β-glycerophosphate. The medium was replaced every 4 days to maintain proper differentiation conditions. On days 7 and 14, the culture supernatant was collected to evaluate ALP activity. Quantification was performed using a commercial diagnostic kit (Hitachi Model 911-AUDIT kit), and absorbance was measured at 450 nm using an ELISA reader.

3.0.2 Alizarin red test

To evaluate calcium mineralization on the scaffold surfaces, an indicator of osteogenic differentiation of HMSCs, a modified Alizarin Red S staining protocol was employed. For each sample, 5000 HMSCs were seeded in 300 µL of culture medium supplemented with 10% FBS directly onto the scaffolds placed in 12-well plates. Cultures were maintained under standard incubation conditions (37 °C, 5% CO_2, 90% humidity). Three wells containing an equivalent number of cells in osteogenic medium without the presence

of scaffolds were considered as controls. After 24 hr, upon confirmation of cell attachment, 1 mL of osteogenic differentiation medium was gently added to each well. The medium was replaced every 4 days throughout the 14-day differentiation period. Following this, the cultures were washed twice with sterile 0.9% sodium chloride (NaCl) solution and fixed using 1% paraformaldehyde for 20 min at room temperature. Samples were then incubated in a 2% (w/v) Alizarin Red S solution (pH = 4.2) for 45 min to stain calcium-rich deposits. After thorough rinsing with NaCl solution to remove excess dye, images were captured using an optical microscope (Hp31, Germany).

3.0.3 Calcium deposition

Quantitative analysis of calcium deposition on PCL/CH and PCL/CH-hPRF scaffolds was performed using a commercial calcium assay kit (Parasazmon, Tehran, Iran) at two time points, day 7 and day 14, post-osteogenic induction. Prior to measurement, the scaffolds were thoroughly rinsed with PBS, followed by the addition of 200 µL of 6% hydrochloric acid (HCl) to each sample. The resulting mixtures were gently pipetted and subjected to vortexing for 40 min at ambient temperature to facilitate calcium extraction. Subsequently, the samples were centrifuged at 12,000 rpm for 15 minutes at 4 °C. The supernatants were carefully collected, and calcium concentrations were determined spectrophotometrically at 570 nm using an ELISA microplate reader (Avecina, Pishtazteb, Iran).

3.1 *In ovo* angiogenic assay in chick embryo

To assess the angiogenic response induced by the scaffolds, an *in ovo* CAM assay was performed using fertilized chicken eggs. The *in ovo* CAM experiments were conducted in accordance with the ethical standards and regulations approved by the Review Board of Medical Sciences of Aliebnabitaleb, Islamic Azad University, Yazd Branch. One-day-old eggs were surface-disinfected with 70% ethanol and incubated at 37 °C with 75% relative humidity. After 7 days of incubation, a 1 × 1 cm window was carefully opened on the eggshell to expose the CAM. A 1 × 2 cm scaffold was gently placed within the prepared window on the eggshell. Each egg received one scaffold, and the procedure was repeated in triplicate. Eggs without any scaffold served as the control group. Each opening was sealed with parafilm, and the eggs were returned to the incubator for an additional 7 days under 90% humidity. On day 14, the embryos were euthanized, and the CAM tissues were harvested for analysis (Fig. 1 (d)). Angiogenesis was evaluated, and the extent of neovascularization was quantified by analyzing vessel density and branching patterns using ImageJ software (v1.51, Java 8). Additionally, CAM samples were fixed and stained with Masson's trichrome to evaluate histological features.

3.2 Statistical analysis

Statistical analysis was conducted using one-way analysis of variance (ANOVA), with significance levels set at $p < 0.05$, $*p < 0.01$, $**p < 0.001$, and $***p < 0.0001$. All experiments were performed in triplicate, and the results are presented as mean ± standard deviation (SD).

4. Results and discussion

Among various fabrication techniques, electrospinning enables the production of scaffolds with a high surface-area-to-volume ratio, tunable porosity, and customizable shapes and dimensions, properties that are favorable for stem cell attachment, proliferation, and differentiation. In this study, a composite scaffold composed of PCL, CH, and hPRF was fabricated via electrospinning and evaluated for its potential in bone tissue regeneration. The incorporation of hPRF, a biologically active component rich in autologous growth factors, was intended to enhance cellular responses and accelerate the osteogenic differentiation of stem cells, thereby promoting faster bone tissue repair.

4.1 Morphology and microstructure of the nanofibers

Figure 2 (a-c) present the SEM images of electrospun PCL, PCL/CH, and PCL/CH-hPRF scaffolds. The normal distribution diagram of the diameter of nanofibers in the scaffolds is shown in figure 2 (d-f). The PCL scaffold exhibits a uniform fibrous morphology with an average fiber diameter of approximately 230 nm and minimal bead formation, indicating stable jet formation under the applied electrospinning parameters. The relatively low flow rate used during electrospinning provided sufficient time for the polymer jet to elongate and solidify before reaching the collector, which is crucial for producing uniform, bead-free fibers. In contrast, higher flow rates tend to result in bead formation or irregular fibers due to premature solvent evaporation and incomplete jet stretching. Upon incorporation of CH into the PCL matrix, a reduction in fiber diameter was observed, with the average diameter decreasing from 230 nm in PCL to 212 nm in the PCL/CH scaffold (Fig. 2 (g)). This change is attributed to the enhanced conductivity of the solution upon the addition of CH, a natural biopolymer with ionic functional groups. The synergistic interaction among PCL, CH, and hPRF arises from hydrogen bonding and electrostatic attractions between their respective functional groups, promoting enhanced structural integrity and mechanical reinforcement within the composite nanofiber scaffold (Fig. 1 (b)). Unlike PCL, which is inherently non-conductive, the inclusion of CH improves the charge-carrying capacity of the solution, resulting in greater stretching of the polymer jet and the formation of thinner fibers under the electric field [19, 41, 42]. Two main mechanisms are proposed to explain the reduction in fiber diameter in the PCL/CH scaffold: (1) the increased electrostatic repulsion among charged polymer chains leads to enhanced elongation and thinning of the fibers; and (2) CH incorporation promotes greater mobility of the polymer chains, facilitating further jet stretching during electrospinning [42, 43]. The morphology of the PCL/CH-hPRF scaffold reveals a mesh-like structure, which is favorable for cellular infiltration and nutrient exchange [26, 44]. Incorporation of hPRF-loaded CH nanoparticles led to a further reduction in fiber thickness, achieving an average diameter of approximately 189 nm in the PCL/CH-hPRF scaffold. Additionally, analysis with MIP software indicated that the CH-hPRF nanoparticles present on the fiber surfaces measured approximately 150 nm in size (Fig. 2 (c)). The integration of CH nanoparticles containing hPRF into

the spinning solution led to a slight increase in viscosity. Within optimal limits, increased viscosity promotes better interaction between polymer chains and solvent molecules, enhancing the uniformity and elongation of the electrospun fibers. In the electrospinning process, balancing solution viscosity and electrical conductivity is essential. Adequate viscosity ensures stable jet formation, while increased conductivity due to the ionic content of CH and hPRF facilitates better charge transfer and fiber stretching, both of which contribute to the formation of thinner, smoother fibers with a higher surface area [45]. In summary, the fiber diameter and morphology in electrospun scaffolds are strongly influenced by the interplay between solution conductivity and viscosity. By optimizing these parameters, scaffolds with uniform, bead-free fibers and desirable architecture for bone tissue engineering applications can be achieved.

The porosity percentages of the scaffolds are illustrated in Fig. 2 (h). Porosity is a key parameter in scaffold design for bone tissue engineering, as it directly influences cell distribution, nutrient diffusion, and tissue in-growth throughout the scaffold matrix [32]. The measured average porosity for the PCL, PCL/CH, and PCL/CH-hPRF scaffolds was 59%, 65%, and 72%, respectively. The increase in porosity observed in the PCL/CH-hPRF scaffold can be attributed to two main factors: the reduction in fiber diameter caused by the improved conductivity and viscosity of the spinning solution, and the incorporation of hPRF-loaded CH nanoparticles, which further enhance the scaffold's surface area and inter-fiber spacing. The presence of these bioactive nanoparticles not only modifies the fiber morphology but also promotes a more open and interconnected network within the scaffold. This high degree of porosity is advantageous for bone tissue regeneration, as it facilitates early-stage cell adhesion, proliferation, and migration. Moreover, the increased surface area supports a more efficient degradation profile and provides a favorable platform for the controlled

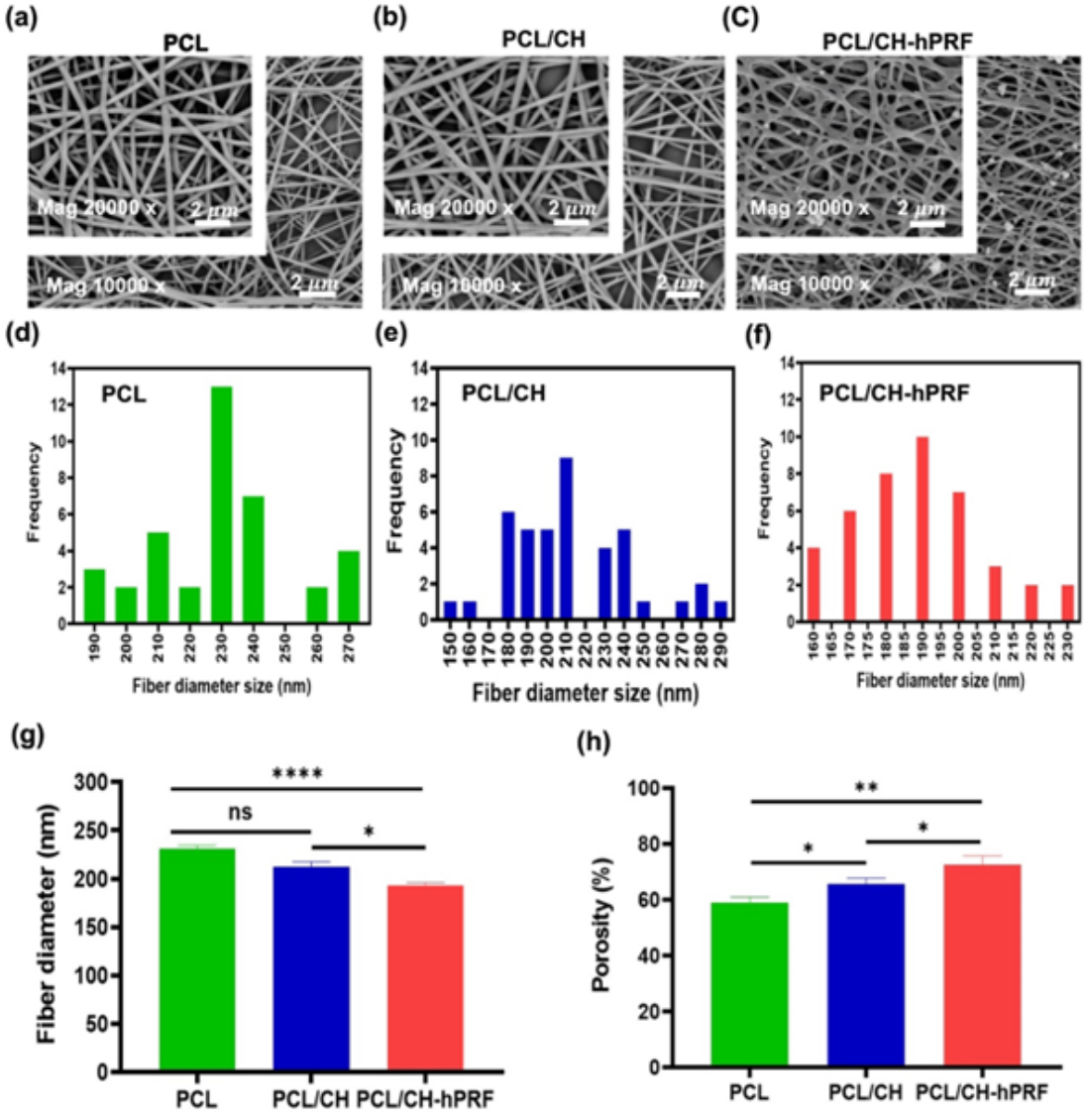

Figure 2. (a-c) SEM micrographs of PCL, PCL/CH, and PCL/CH-hPRF scaffolds at different magnifications; (d-f) Fiber size distribution in the scaffolds; (g) Fiber diameter of the scaffolds; and (h) Porosity percentage of the scaffolds. Statistical significance: ****$p < 0.0001$, **$p < 0.01$, *$p < 0.05$, and ns = not significant.

release of growth factors encapsulated within the scaffold. The porous architecture of the PCL/CH-hPRF composite scaffold thereby offers an environment conducive to rapid stem cell differentiation and bone matrix deposition [44].

Figure 3 presents the FTIR spectra of PCL, CH, CH-hPRF nanoparticles, and the PCL/CH-hPRF scaffold in the spectral range of $400 - 14000\ cm^{-1}$. In the PCL spectrum, characteristic absorption bands are observed between $3100 - 3300\ cm^{-1}$, corresponding to the C−H stretching vibrations. Additional notable peaks at $1167\ cm^{-1}$ and $1630\ cm^{-1}$ are attributed to the stretching of O-C-O and C=O bonds within the ester functionalities of the polymer backbone, respectively [19, 32]. In the CH spectrum, prominent peaks at $3600\ cm^{-1}$ indicate the stretching vibrations of N-H and O-H groups, while a signal near $2924\ cm^{-1}$ is associated with aliphatic C-H bonds. Moreover, absorption bands around $1592\ cm^{-1}$ and $1400\ cm^{-1}$ are related to amide I and CH_2 bending, respectively. A smaller peak near $754\ cm^{-1}$ corresponds to saccharide ring structures characteristic of CH [45, 46]. The spectral features of CH-hPRF nanoparticles retain all major CH-related bands, confirming the preservation of the CH structure. Furthermore, absorption bands at $1680\ cm^{-1}$ and $1530\ cm^{-1}$ in this spectrum are associated with aromatic ring vibrations, reflecting the presence of hPRF [47]. In the FTIR spectra of the PCL/CH-hPRF scaffold, all signature peaks corresponding to its individual components are identifiable, indicating the successful incorporation of PCL, CH, and hPRF without any significant chemical modifications. The absence of new absorption bands further suggests that no covalent interactions occurred between the phases, and the original chemical structures of the composite materials have remained intact during the scaffold fabrication process.

4.2 Physical Features of the scaffolds

One of the key parameters influencing scaffold performance in tissue engineering is surface hydrophilicity, as it plays a vital role in supporting cell adhesion, growth, migration, and differentiation processes. In this study, a dynamic contact angle measurement, including both advancing and receding angles, was employed to obtain a more accurate assessment of the wettability of the porous nanofiber scaffolds. Compared with static contact angle measurement, this method minimizes errors caused by liquid penetration into the scaffold's pores and more accurately captures realistic wetting behavior [48, 49]. Figure 4 (a) illustrates mean contact angle (θ), advancing angle (θ_a), and receding angle (θ_r) for the scaffolds. The difference between the advancing and receding contact angles reflects the overall wettability characteristics of the scaffolds. The mean contact angles for PCL, PCL/CH, and PCL/CH-hPRF scaffolds were determined to be approximately 68.21°, 45.07°, and 32.27°, respectively. The significant decrease in angle within the PCL/CH-hPRF scaffold reflected an improvement in surface swelling associated with the presence of hPRF-loaded CH particles. Table 1 presents the average contact angles and weight changes for the scaffolds. The measured weight changes for the PCL, PCL/CH, and PCL/CH-hPRF scaffolds were 0.17 g, 0.20 g, and 0.26 g, respectively. Greater weight change in PCL/CH-hPRF indicated higher hydrophilicity, as increased water uptake reflects improved interaction between the liquid and the scaffold surface and its interconnected pores. The contact angle (θ) decreased from 68.21° for PCL to 32.27° for PCL/CH-hPRF, further confirming that the incorporation of hPRF into the composite enhanced the scaffold's surface wettability. A lower contact angle indicates enhanced hydrophilicity and greater dynamic contact angle hysteresis, often linked to increased porosity and decreased fiber diameters. CH, a naturally derived polymer rich in hydrophilic functional groups such as hydroxyl (-

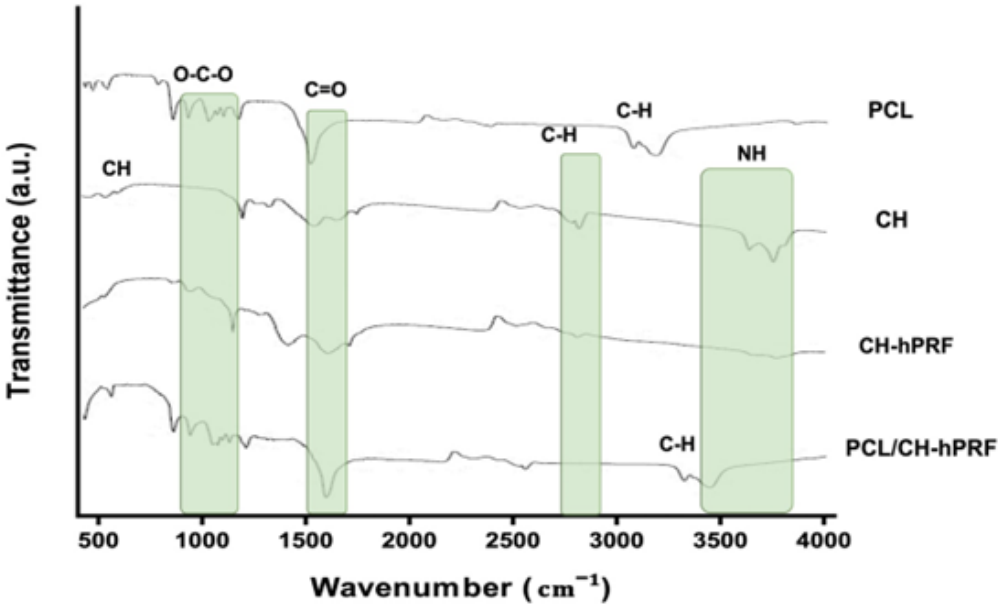

Figure 3. FTIR spectra of PCL, CH, CH-hPRF nanoparticle, and PCL/CH-hPRF scaffold.

OH), contributes significantly to increased water affinity when incorporated into scaffold formulations. As the CH content rises, so does the scaffold's hydrophilicity [17, 27, 43]. Moreover, integrating CH-based nanoparticles containing hPRF led to a reduction in fiber diameter, increasing of specific surface area, and greater scaffold porosity, all contributing to a further reduction in the water contact angle. The enhanced porosity and smaller fiber diameter of the PCL/CH-hPRF scaffold also resulted in a greater weight difference during swellability test, suggesting higher water uptake capacity [27, 50]. These characteristics are closely linked to the scaffold's ability to the cell-scaffold interactions, potentially leading to improved cell adhesion, proliferation, and differentiation outcomes.

Biodegradable materials are widely favored in biomedical applications, primarily due to their ability to naturally degrade within the body, eliminating the need for surgical removal after implantation. The rate at which these materials degrade is strongly influenced by factors such as hydrophilicity, molecular weight, crystallinity, and the overall composition of the material. An imbalance in this degradation rate can be detrimental; overly slow degradation may hinder tissue regeneration by physically impeding new tissue growth, while an abnormally rapid breakdown can compromise the scaffold's mechanical integrity and the controlled release of therapeutic agents. As a result, accurate assessment of scaffold degradability is critical in the development of tissue-engineered constructs [3]. Figure 4 (b) illustrates the degradation behavior of the scaffolds over a 6-week immersion period in PBS. After this duration, the degradation percentages were calculated to be approximately 48%, 40%, and 35% for the PCL/CH-hPRF, PCL/CH, and PCL scaffolds, respectively. The enhanced degradation observed in the PCL/CH-hPRF scaffold is likely attributed to the hydrophilic nature of CH and its tendency to swell in aqueous environments, which can disrupt key intermolecular interactions such as hydrogen and amide bonds [43]. Furthermore, the inclusion of hPRF-loaded CH nanoparticles led to a reduction in nanofiber diameter, an increase in specific surface area, and a higher porosity level, features that contribute to improved PBS penetration during degradation testing. As the PBS solution infiltrates the scaffold structure, polymer chains undergo disintegration, resulting in noticeable weight loss over time [51]. The degradation trend showed a marked increase during the first two weeks, followed by a plateau phase up to week 6. figure 4 (c-d) show the morphology of the PCL/CH-hPRF scaffold after prolonged immersion in PBS

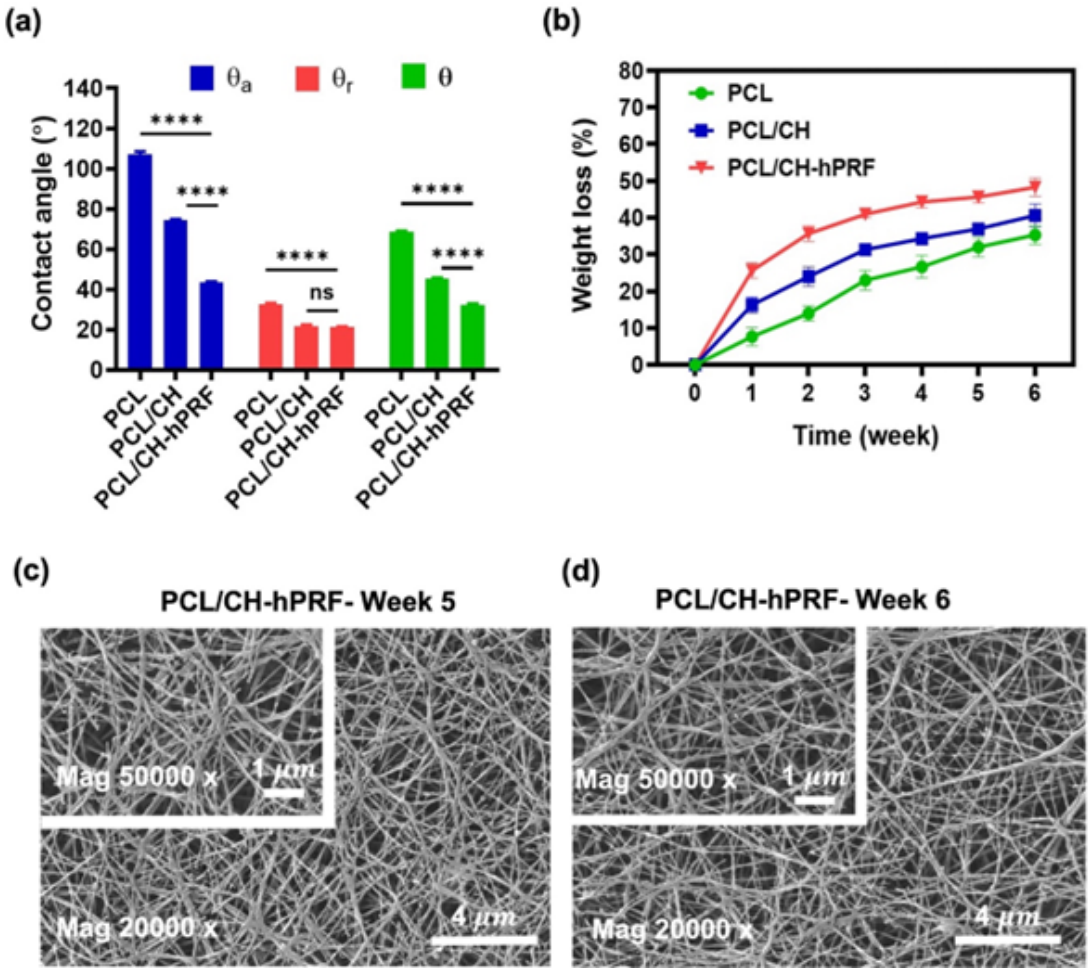

Figure 4. (a) Average contact angle (θ), advancing contact angle (θ_a), and receding contact angle (θ_r) of the scaffolds, (b) Weight loss profile of the scaffolds over a 6-week degradation period; and (c-d) SEM images showing the morphological changes of the PCL/CH-hPRF scaffold at weeks 5 and 6 following PBS immersion. Statistical significance: ****$p < 0.0001$ and ns = not significant.

Table 1. Mean contact angle (θ), advancing angle (θ_a), receding angle (θ_r), and weight changes (Δw) of the scaffolds.

Scaffold	θ (degrees)	θ_r (degrees)	θ_a (degrees)	Δw (g)
PCL	68.21	32.87	107.55	0.17
PCL/CH	45.07	21.83	74.31	0.20
PCL/CH-hPRF	32.27	21.23	43.31	0.26

for 5 and 6 weeks. SEM images for the PCL and PCL/CH scaffolds are not presented. Their lower weight loss and slower degradation rate compared with the PCL/CH-hPRF scaffold suggest that they would likely retain their fibrous morphology and overall structural integrity after 6 weeks of PBS immersion. Partial degradation of nanofibers, the scaffold maintained its original form to a large extent over this period, suggesting a steady yet controlled degradation profile suited for sustained tissue support. Despite the weight loss measurements indicating substantial degradation (48%) for the PCL/CH-hPRF after 6 weeks, the SEM images show that the fibrous structure and overall scaffold architecture remain largely intact. This phenomenon aligns with previous studies where polymer scaffolds experience significant degradation within internal and superficial regions, leading to noticeable weight loss, yet retain their external morphology [52]. The observed decrease in scaffold weight stems from the breakdown of amorphous polymer zones, the release of low-molecular-weight fragments, or dissolution processes. These changes often occur without immediate, visible alterations at the microscale level. Furthermore, early degradation stages typically involve hydrolytic cleavage inside the polymer matrix, chain fragmentation, surface erosion, and enlargement of pores. Pronounced weight loss can thus precede any clear morphological deterioration or fiber fragmentation [53]. Published studies [52, 54] corroborate that many electrospun polymer scaffolds can lose a significant fraction of their weight, commonly between 30% and 50%, while still preserving a coherent fibrous network and scaffold form. This retention of mechanical structure is attributed to the endurance of crystalline or less hydrolyzed polymer segments.

4.3 Mechanical properties of the scaffolds

For bone tissue engineering applications, scaffolds must possess adequate mechanical properties, including tensile strength and elastic modulus, to support cellular adhesion, proliferation, and subsequent differentiation, ultimately enabling effective tissue regeneration [55]. Optimizing mechanical behavior is particularly important to maintain scaffold integrity post-implantation, delay premature structural failure, and ensure a synchronized degradation profile with the timeline of new tissue formation. The mechanical response of electrospun scaffolds can be influenced by several factors, including polymer composition, fiber diameter, morphology, and overall uniformity of the fiber network [56]. In this study, uniaxial tensile tests were conducted along the direction of the aligned fibers to evaluate mechanical behavior. Key tensile parameters extracted from this test are summarized in Table 2, while corresponding stress-strain curve and quantified values of tensile strength and failure strain of the scaffolds are depicted in Figs. 5 (a-d). The measured tensile stress for PCL, PCL/CH, and PCL/CH-hPRF scaffolds was 3.31, 2.05, and 2.17 MPa, respectively. Failure strain was recorded at 28.66%, 13.42%, and 9.08% for the same groups. Notably, the elastic modulus values were 35.53, 40.44, and 45.35 MPa, indicating a progressive increase in stiffness upon the incorporation of CH and hPRF. Among the tested scaffolds, the PCL scaffold displayed the highest failure strain, which is attributable to its thicker fibers and relatively lower porosity, factors that typically enhance ductility. As previously reported by Bölgen et al. [57], an increase in fiber diameter is positively correlated with higher tensile strength. Meanwhile, reducing the polymer concentration during electrospinning has been shown to reduce mechanical integrity [56, 58]. Interestingly, while the addition of CH decreased tensile strength due to increased porosity and reduced fiber diameters, incorporating hPRF nanoparticles partially restored this strength by reinforcing the matrix [56]. Hence, the tensile performance of the PCL/CH-hPRF scaffold slightly exceeded that of the binary PCL/CH scaffold. In contrast to tensile strength trends, the elastic modulus followed an ascending pattern from PCL to PCL/CH and reached its highest value in the PCL/CH-hPRF scaffold. This is likely a result of the finer fiber network and enhanced stiffness contributed by hPRF-loaded CH nanoparticles. According to Kwon et al. [59], as fiber thinness increases, so does the modulus of elasticity, which aligns with the observed improvements. Similar findings regarding the stiffness enhancement of PCL-based scaffolds following CH incorporation have also been reported [19, 56, 60].

Table 2. Mechanical properties of the scaffolds obtained from uniaxial tensile testing.

Scaffold	Tensile Stress (Mpa)	Failure Strain (%)	Elastic Modulus (Mpa)
PCL	3.31	28.66	35.53
PCL/CH	2.05	13.42	40.44
PCL/CH-hPRF	2.17	9.08	45.35

4.4 *In vitro* drug releas

Tracking the amount of drug released over time supports the development of delivery systems with controlled and prolonged release profiles, thereby enhancing therapeutic outcomes while limiting unwanted side effects [61]. The release behavior of hPRF from CH-hPRF nanoparticles and from PCL/CH-hPRF nanofibers was monitored over a 14-day period. The encapsulation efficiencies (EE) for CH-hPRF nanoparticles were determined to be 58%. The cumulative release profiles of hPRF from both systems are presented in Fig. 6 (a). Analysis of these curves revealed three distinct release phases: (1) an initial burst phase; (2) a swelling-driven stage whereby PBS penetrates the matrix and allows hPRF to diffuse outward over several days; and (3) a final stage dominated by polymer erosion and degradation [36]. During the first hour, the released hPRF amounted to approximately 7.58% (1.21 µg/µL) for CH-hPRF nanoparticles and 5.45% (0.87 µg/µL) for PCL/CH-hPRF nanofibers scaffold, indicating that the scaffold structure substantially reduced the early burst release. The higher initial release from CH-hPRF nanoparticles is attributed to the presence of hPRF on the surface of CH-hPRF nanoparticles. After 14 days, cumulative release reached 39.32% (6.29 µg/µL) for CH-hPRF nanoparticles and 31.25% (5.00 µg/µL) for the nanofibers scaffold, confirming the ability of the latter to sustain a slower and more prolonged release profile. For comparison, Abazari et al. [62] developed a platelet-rich plasma (PRP) /polyvenilalcohol/CH/hydroxyapatite nanofibrous scaffold to enhance osteogenic differentiation and bone regeneration, reporting that PRP release after 10 days in PBS reached approximately 60%. In another study [63], a PRP-loaded hydrogel was formulated for osteoarthritis therapy. The release behavior displayed a distinct two-phase trend, starting with a rapid, short-term discharge of proteins, followed by a slower, prolonged release. Measurements showed that roughly 40% of the total protein content diffused out within the first 2.5 hours. By day 6, the cumulative release had reached nearly 80%. The release then advanced gradually for the next several days, completing in around 10 days. This sequence suggests that the formulation delivers an initial surge of bioactive molecules, while the hydrogel network progressively degrades to maintain a sustained supply over time. In contrast, the current findings demonstrate that hPRF release from the PCL/CH-hPRF scaffold followed a gradual, sustained pattern over the same period, reflecting the efficacy of the design in modulating growth factor release kinetics.

Figure 6 (b) displays the hPRF release profile in PBS (pH:7.4) for CH-hPRF nanoparticles and PCL/CH-hPRF scaffold evaluated using the Higuchi model. The cumulative amount released (y) is plotted against the square root of time (x), consistent with a diffusion-driven process. Correlation coefficients (R^2) above 0.97 were obtained for both the initial and extended release periods, demonstrating a high level of consistency between the measured data and the model output [37, 64]. The Higuchi constants (KH), derived from

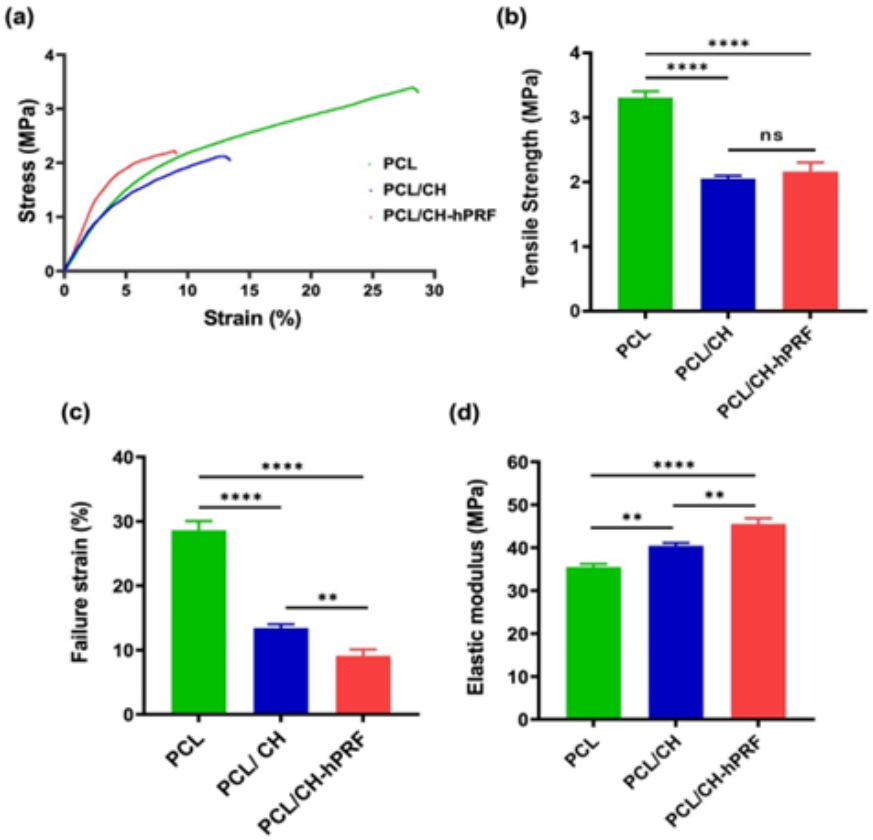

Figure 5. (a) Representative stress–strain curves; (b) Tensile strength; (c) Failure strain; and (d) Elastic modulus for the PCL/CH and PCL/CH-hPRF scaffolds. Statistical significance: ****p < 0.0001, **p < 0.01, and ns = not significant.

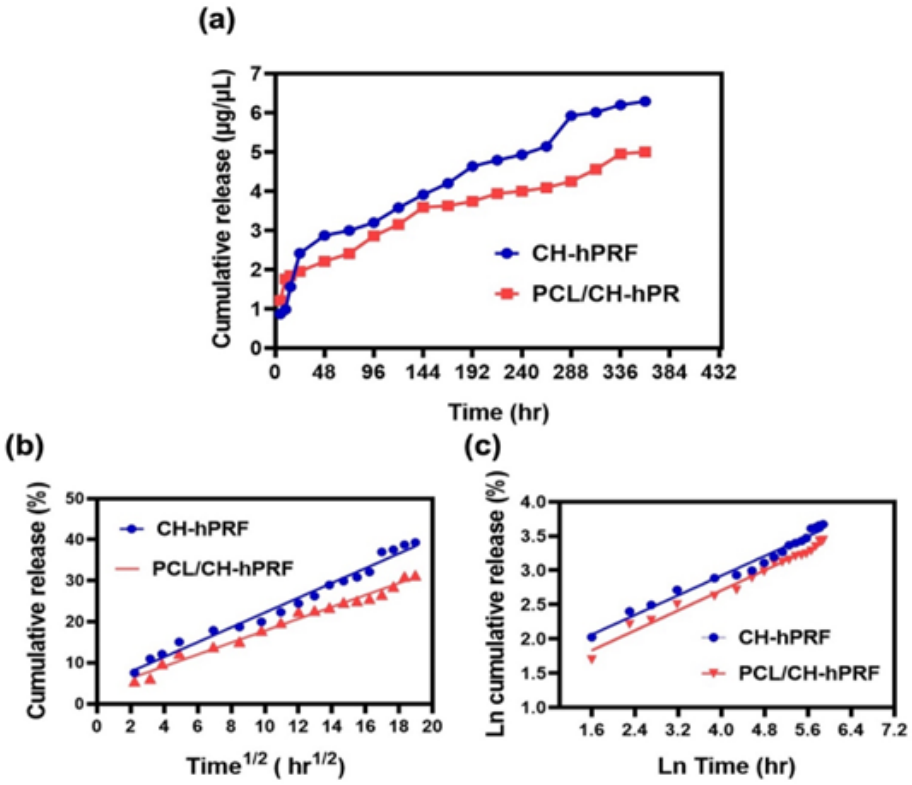

Figure 6. (a) Cumulative release profile of hPRF from CH-hPRF nanoparticles and PCL/CH-hPRF nanofibrous scaffolds over time; Drug release profiles of CH-hPRF nanoparticles and PCL/CH-hPRF nanofibrous scaffolds fitted using (b) the Higuchi model and (c) the Ritger-Peppas model.

slope values of 1.79 for CH-hPRF nanoparticles and 1.44 for the PCL/CH-hPRF scaffold, reflect the rate at which hPRF diffuses through the nanoparticle and nanofibrous scaffold based on the Higuchi model. The high correlation coefficients ($R^2 = 0.98$) for CH-hPRF and PCL/CH-hPRF indicated a strong linear fit of the data to the model. Despite this linearity, the overall release pattern suggests that mass transport was driven by a Fickian mechanism. Applying the Ritger-Peppas model for the samples (Fig. 6 (c)) also produced a very good fit, with $R^2 = 0.97$ for CH-hPRF nanoparticles and $R^2 = 0.98$ for PCL/CH-hPRF scaffold. The corresponding release exponents were $n = 0.35$ for the nanoparticles and $n = 0.36$ for the scaffold (Table 3). Since both values are below the 0.43 limit, the dominant release mechanism can be attributed to Fickian diffusion. Taken together, the findings from the two kinetic models indicated that hPRF liberation from both carriers proceeds primarily through a diffusion-controlled process, enabling sustained and regulated release that can be advantageous for bone regeneration applications.

4.5 Surface bioactivity

The formation of a stable biological interface between implanted scaffolds and native bone tissue depends strongly on the bioactivity of the biomaterial, which refers to its ability to support the nucleation and growth of bone-like apatite in physiological conditions. To investigate this property, the bioactivity of PCL, PCL/CH, and PCL/CH-hPRF scaffolds was assessed following immersion in SBF for 28 days. Figures 7 (a-c) present FESEM micrographs of the scaffold surfaces after 28 days of immersion in SBF solution. Among the studied samples, the PCL/CH and PCL/CH-hPRF scaffolds exhibited a more prominent deposition of apatite compared to PCL scaffold, as evident by the denser coverage of mineralized layers on their surfaces. The enhancement in mineralization for the composite scaffolds can be linked to the increased surface reactivity resulting from the functional groups introduced by CH and hPRF components. Quantitative analysis of ion concentrations in the SBF medium was carried out using ICP, as illustrated in Fig. 7 (d). Over the entire incubation period, a noticeably lower calcium concentration was observed

Table 3. Release parameters of CH-hPRF nanoparticles and PCL/CH-hPRF scaffold as calculated using the Higuchi and Ritger-Peppas kinetic model.

Scaffold	Higuchi Equation				Ritger-Peppas Equation			
	Eq.	$K_{H\ theory}$	K_H	R^2	Eq.	K	n	R^2
CH-hPRF	Y = 1.799x + 4.271	2.07	1.79	0.9807	Y = 0.3585x + 1.490	4.43	0.35	0.9766
PCL/CH-hPRF	Y = 1.447x + 3.383	1.64	1.44	0.9838	Y = 0.3653x + 1.248	3.48	0.36	0.9827

in the supernatant of the PCL/CH-hPRF group, suggesting higher rates of calcium uptake and mineral deposition compared to PCL and PCL/CH scaffolds. PCL inherently contains -COOH and -OH groups, which provide sites for the adsorption of calcium ions, subsequently facilitating the nucleation of phosphate ions and the formation of apatite crystals [4]. The introduction of CH further contributes to this process, as its protonated amine groups ($-NH_3^+$) can attract negatively charged phosphate ions and promote apatite layer development [65]. In the case of the PCL/CH-hPRF scaffold, the bioactivity is further enhanced by the incorporation of PRF, which contains biofunctional moieties such as free $-NH_2$ groups that act as additional nucleation centers for calcium ion binding. This synergistic effect leads to greater apatite precipitation and denser mineral coverage [66]. The PCL/CH-hPRF scaffold exhibited a greater formation of apatite-like deposits compared to the other scaffolds, attributable to the presence of CH-hPRF nanoparticles. Overall, the data confirm that the PCL/CH-hPRF scaffold demonstrated superior bioactivity and biomineralization potential over the 28-day period, outperforming PCL and PCL/CH scaffolds in mimicking bone-like apatite formation *in vitro*.

4.6 Cellular response and protein adsorption

Figure 8 (a) illustrates the viability and proliferation of osteoblast-like cells cultured on PCL/CH and PCL/CH-hPRF scaffolds after 72 hr. A noticeably higher rate of cell proliferation was observed on the PCL/CH-hPRF scaffold compared to the PCL/CH group. Based on quantitative analysis, the cell viability percentages were 105% for PCL/CH and 120% for PCL/CH-hPRF scaffolds. The improved cell response on the ternary scaffold is mainly attributed to its finer fiber network and enhanced porosity, which collectively promote nutrient diffusion and surface area for cell-material interactions [56]. Beyond architectural features, the material composition also plays a critical role in cell behavior. The incorporation of CH within the PCL matrix increases hydrophilicity, which positively impacts initial cell attachment and supports extended proliferation [50]. Furthermore, the addition of hPRF contributes bioactive growth factors, such as IGF and PDGF, which are known to amplify osteoblast migration and stimulate mitotic activity [50, 67]. These specific biomolecules enhance the regenerative potential and cellular activity on the scaffold [68, 69]. The adhesion characteristics of osteoblasts were further examined via SEM imaging, as presented in Figs. 8 (b-c). After three days of culture, cells on both scaffold types exhibited flattened morphologies and well-developed pseudopodia. However, cell coverage on the PCL/CH-hPRF scaffold was more extensive, nearly forming a confluent layer. This behavior implied enhanced cellular affinity for the surface, likely due to the presence of functional amine and hydroxyl groups from CH and hPRF, which contribute to surface hydrophilicity and protein adsorption [70]. Additionally, the fine fiber morphology facilitates better interfacial contact

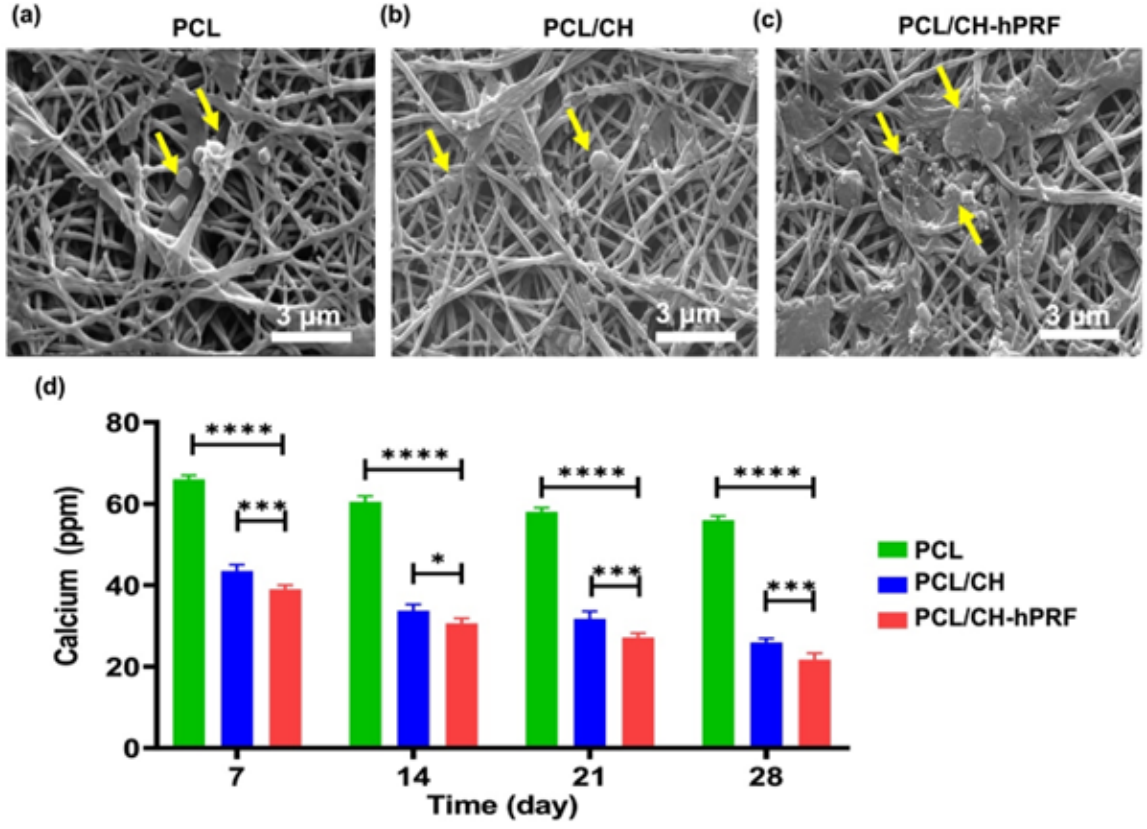

Figure 7. (a-c) FESEM micrographs of scaffold surfaces after immersion in SBF solution for 28 days. Yellow arrows indicate areas of mineralization and apatite-like precipitate formation and (d) Calcium ion concentration in the supernatant of SBF after 7, 14, 21, and 28 days of scaffold incubation.Statistical significance: ****$p < 0.0001$, ***$p < 0.001$, *$p < 0.05$.

for adhering cells [56, 71, 72]. The improved protein adsorption on PCL/CH-hPRF scaffolds further supports these observations.

Protein adsorption is a critical preliminary step in cell attachment, influencing adhesion and subsequent morphology [73]. As shown in Fig. 8 (d), the control sample exhibited minimal protein retention (12 μg/mm^3), while adsorption levels significantly increased to 40 μg/mm^3 and 51 μg/mm^3 for PCL/CH and PCL/CH-hPRF scaffolds, respectively. This enhancement is attributed not only to the presence of hydrophilic components (Fig. 4 (a)) but also to the reduction in fiber diameter and the resultant elevation in specific surface area, both of which facilitate greater protein-surface interaction [40, 74]. Collectively, the synergistic effects of structural features, chemical composition, and biological additives in the PCL/CH-hPRF scaffold establish a favorable environment for cellular attachment, proliferation, and differentiation, highlighting its potential in bone tissue engineering applications

4.7 Osteogenic differentiation of HMSCs

The osteogenic differentiation of HMSCs was assessed by measuring ALP activity at days 7 and 14 of culture. ALP is a key early-stage marker for osteoblast differentiation and is commonly used to evaluate the progression of stem cells toward an osteogenic lineage [75]. Quantitative results of ALP activity are presented in Fig. 8 (e). The control group, which consisted of HMSCs cultured in osteogenic medium without scaffold materials, showed ALP activity levels of 28 U/L on day 7 and 40 U/L on day 14. In comparison, PCL/CH scaffolds induced ALP activity of 40 U/L and 60 U/L on days 7 and 14, respectively. The PCL/CH-hPRF scaffolds demonstrated the highest levels, with 43 U/L on day 7 and 78 U/L on day 14. These findings indicated a progressive increase in osteogenic activity over time, with both scaffold types supporting enhanced ALP expression relative to the control. Although no statistically significant difference was observed between the scaffold groups on day 7, the trend changed considerably by day 14. The PCL/CH-hPRF scaffold showed a markedly higher ALP activity, suggesting a superior osteoinductive effect. This enhancement can be attributed to the presence of CH, which has been shown to suppress osteoclastogenesis while promoting the upregulation of osteogenic markers such as osteopontin and type I collagen [7]. In addition, the incorporation of hPRF into the scaffold likely contributed to elevated ALP activity through the sustained release of osteoinductive cytokines and growth factors. These include BMPs, VEGF, IGF, TGF-β1, and PDGF, all of which are known to play critical roles in accelerating HMSCs proliferation, differentiation, and extracellular matrix mineralization [76–79].

The accumulation of calcium-rich mineral deposits is considered a sign of osteogenic differentiation and is strongly associated with the presence of mature osteoblasts [26, 75]. To qualitatively and quantitatively assess this process, surface staining with Alizarin Red S as a dye that selectively binds to calcium ions was performed. As mineralized matrix increases, so does the intensity and distribution of red staining across the scaffold surface, thereby offering a visual and measurable indication of osteogenesis [80, 81]. In this study, Alizarin Red S staining was conducted on day 14 for PCL/CH and PCL/CH-hPRF composite scaffolds, alongside a control group consisting of cells cultured in osteogenic medium without scaffolds. As shown in Fig. 8 (f), the extent of mineralized surface, inferred from the stained area, was approximately 5% for the control group, 30% for PCL/CH, and 40% for the PCL/CH-hPRF scaffold. In addition, Fig. 8 (g-m) depict the distribution of calcium deposits visually on the scaffold surfaces. Notably, minimal staining was observed in the control group, indicating limited mineralization in the absence of scaffold support. The superior calcium accumulation observed in the PCL/CH-hPRF group can be attributed to both the bioactive composition of the scaffold and its surface characteristics. The presence of amino groups in chitosan enhances calcium ion binding [26], while the incorporation of hPRF introduces a fibrin network rich in osteoinductive growth factors such as PDGF, VEGF, and TGF-β1 [82]. These biological signals are known to facilitate HMSCs proliferation, differentiation, and matrix mineralization.

Further quantitative analysis of calcium content was performed on days 7 and 14, as shown in Fig. 8 (n). On day 7, calcium deposition levels were determined to be 10 μg/scaffold in the control group, 20 μg/scaffold for PCL/CH, and 30 μg/scaffold for PCL/CH-hPRF. By day 14, these values rose to 25, 30, and 40 μg/scaffold, respectively. Both composite scaffolds exhibited significantly greater calcium deposition than the control, with the PCL/CH-hPRF scaffold demonstrating a statistically significant increase even over the PCL/CH group. Such an enhancement underscores the role of PRF-derived bioactive components and surface modifications in promoting mineralization. Taken together, the combination of CH and hPRF in the composite scaffold not only supports stem cell adhesion and proliferation but also accelerates osteogenic differentiation through enhanced calcium-binding capacity and bioactive signaling [50]. These observations highlight the potential of the PCL/CH-hPRF scaffold as a promising candidate for bone tissue regeneration and defect repair.

4.8 Angiogenesis in chick embryo CAM model

The formation of functional blood vessels plays a central role in supplying oxygen and nutrients to engineered tissues while facilitating the removal of metabolic waste, factors essential for the long-term viability of implanted scaffolds [83]. To assess the angiogenic capacity of the developed scaffolds, the CAM assay was employed on the control, PCL, PCL/CH and PCL/CH-hPRF groups. As depicted in Fig. 9 (a), the PCL/CH-hPRF scaffold demonstrated angiogenic activity in the *in ovo* model, with a notably enhanced vascular response in the presence of hPRF. Quantitative analysis revealed that the number of blood vessels formed following implantation was approximately 39 for control, 44 for PCL, 55 for PCL/CH and 187 for PCL/CH-hPRF scaffolds (Fig. 9 (b)), indicating that the hPRF-containing scaffold promoted a 3.4-fold increase in vessel formation compared to the hPRF-free scaffold. The enhanced vascularization observed in the PCL/CH-hPRF group can be

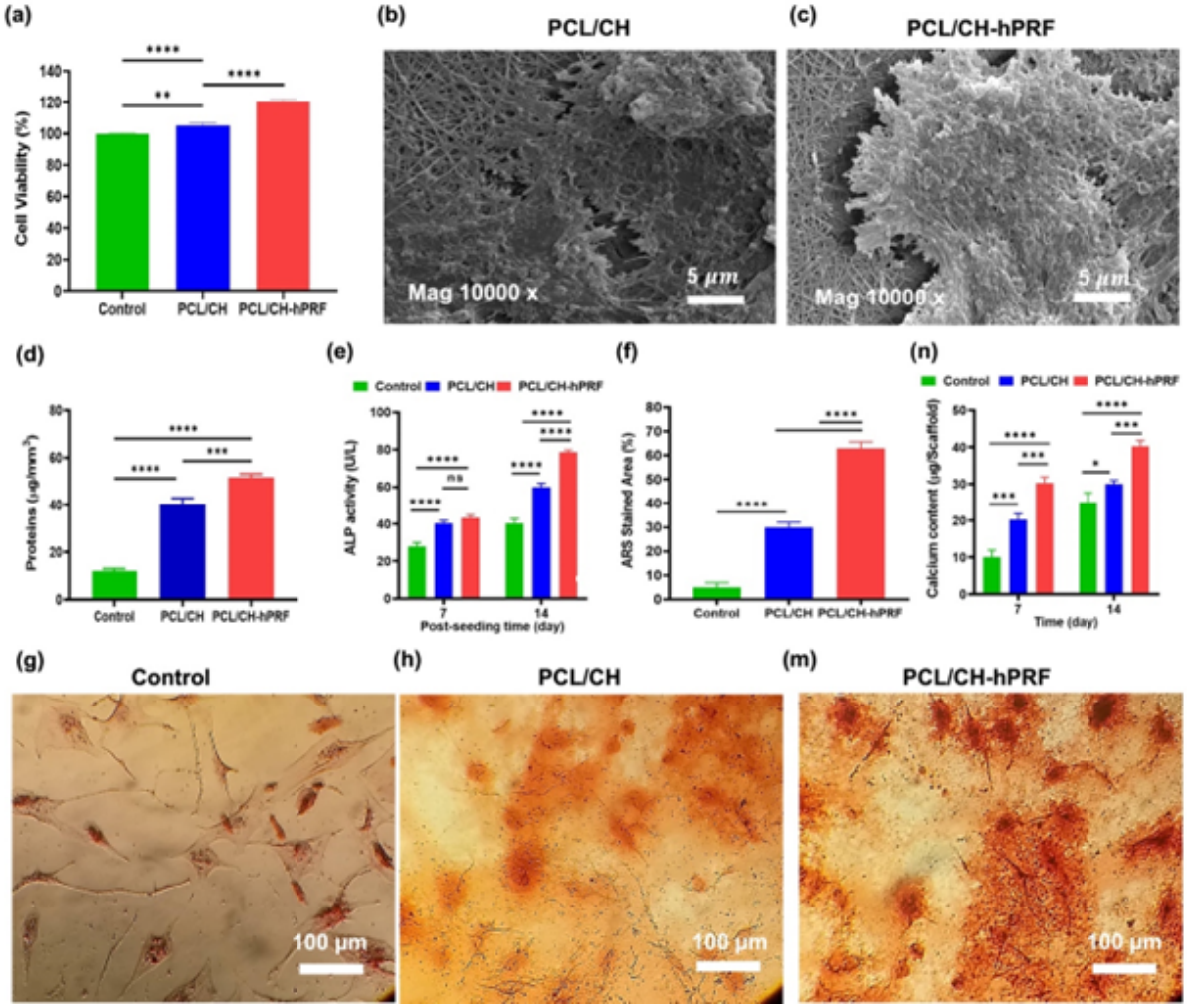

Figure 8. (a) Proliferation profile of MG-63 cells after 72 hr of culture on the scaffold surfaces and control sample; (b-c) SEM micrographs illustrating the morphology and adhesion of MG-63 cells after 72 hr of incubation on the scaffold surfaces; (d) Protein adsorption levels measured on PCL/CH and PCL/CH-hPRF composite scaffold surfaces; (e) Quantitative analysis of ALP activity in the scaffolds, and control group on days 7 and 14; (f) Alizarin Red S (ARS) positive area indicating mineralized calcium-rich regions after 14 days of cell culture; (g-m) Optical microscopy images of ARS-stained scaffold surfaces on day 14; and (n) Calcium deposition on the surface of composite scaffolds and control sample on day 14 and 7. Statistical significance: ****$p < 0.0001$, ***$p < 0.001$, **$p < 0.01$, *$p < 0.05$, and ns = not significant.

linked to the synergistic bioactivity of CH and hPRF components. These biomolecules appear to stimulate endothelial cell adhesion, migration, and proliferation, critical steps in the angiogenic cascade [84]. Specifically, CH is known to support cytoskeletal reorganization, while hPRF provides a reservoir of pro-angiogenic factors that influence endothelial cell behavior and vascular sprouting [85, 86].

Histological sections stained with Masson's trichrome are shown in Fig. 9 (c), illustrating differences in CAM morphology across the groups. Notably, thicker CAM layers were detected in the PCL/CH-hPRF group, which is suggestive of increased fibroblast activity, collagen deposition, and ECM remodeling. This outcome aligns with the known bioactive profile of hPRF, which includes VEGF capable of stimulating endothelial cell activation, along with PDGF, known to promote vessel stabilization and maturation [87, 88]. Collectively, these findings demonstrate that among the studied scaffolds, the PCL/CH-hPRF composite exhibited the most robust pro-angiogenic capacity. The combination of favorable surface hydrophilicity and sustained release of angiogenic cytokines positions it as a promising candidate for promoting vascular integration in bone tissue engineering applications.

5. Conclusion

In this study, composite scaffolds based on PCL/CH and PCL/CH-hPRF were successfully fabricated using electrospinning, and the influence of hPRF-loaded CH nanoparticles on scaffold morphology, mechanical performance, and biological behavior was systematically investigated. Incorporation of these bioactive nanoparticles led to a reduction in fiber diameter and a noticeable increase in scaffold porosity, hydrophilicity, and biodegradation rate compared to the PCL and PCL/CH scaffolds. The addition of hPRF not only enhanced the mechanical properties of the composite scaffold but also significantly improved its biological performance. The release profile of hPRF from the PCL/CH-hPRF scaffold exhibited a gradual and sustained pattern. Cellular assays demonstrated a considerable increase in osteoblast viability, attachment, and

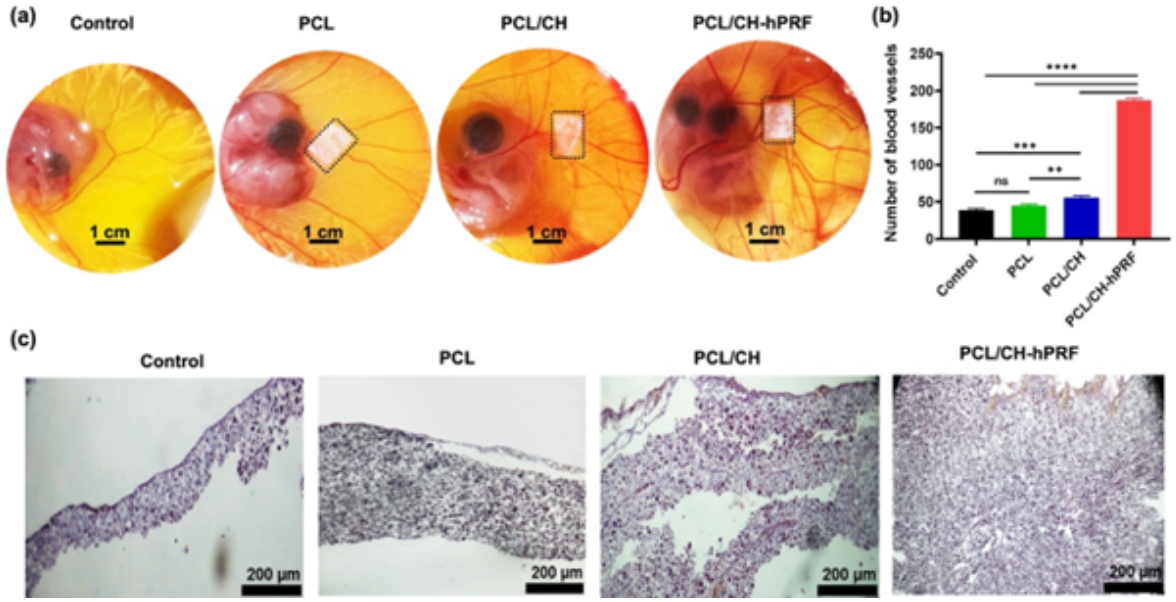

Figure 9. Chick embryo CAM assay. (a) Photographs of the control group and the scaffolds groups, which were loaded on the CAMs on day 14 of incubatio; (b) Quantitative analysis of blood vessel density induced by the scaffolds; and (c) Representative histological images of CAM tissues stained with Masson's trichrome, showing scaffold-induced changes in membrane thickness, collagen deposition, and vascular development. Statistical significance: ****$p < 0.0001$, ***$p < 0.001$, **$p < 0.01$, and ns = not significant.

proliferation on the PCL/CH-hPRF surface, supported by elevated protein adsorption. The presence of hPRF-derived growth factors contributed to greater bioactivity, as reflected by increased ALP enzyme activity, accelerated calcium mineralization, and enhanced osteogenic differentiation of human mesenchymal stem cells. Furthermore, the *in ovo* CAM assay confirmed the angiogenic potential of the hPRF-containing scaffold, evidenced by higher blood vessel formation and increased CAM membrane thickness. Collectively, the simultaneous stimulation of osteogenesis and angiogenesis underscores the promising potential of the PCL/CH-hPRF composite scaffold for use in bone tissue engineering and the regeneration of critical-sized bone defects.

Acknowledgments

The authors would like to express their sincere gratitude to the Islamic Azad University, Yazd Branch, for its valuable support.

Authors contributions

All authors contributed equally to the conception, design, execution, and writing of this work. All authors read and approved the final manuscript.

Availability of data and materials

The datasets generated during and/or analyzed during the current study are available from the corresponding author on reasonable request.

Conflict of interests

The authors declare that they have no known competing financial interests or personal relationships that could have appeared to influence the work reported in this paper.

References

[1] Tang, D., Tare, R. S., Yang, L.-Y., Williams, D. F., Ou, K.-L., and Oreffo, R. O. "Biofabrication of bone tissue: approaches, challenges and translation for bone regeneration." *Biomaterials* **83**:pp. 363–382, pp. 363–382

[2] Denry, I. and Kuhn, L. T. "Design and characterization of calcium phosphate ceramic scaffolds for bone tissue engineering." *Dental Materials* **32**(1):pp. 43–53, pp. 43–53

[3] Lu, H.-T., Lu, T.-W., Chen, C.-H., and Mi, F.-L. "Development of genipin-crosslinked and fucoidan-adsorbed nano-hydroxyapatite/hydroxypropyl chitosan composite scaffolds for bone tissue engineering." *International journal of biological macromolecules* **128**:pp. 973–984, pp. 973–984

[4] Tohidlou, H., Shafiei, S. S., Abbasi, S., Asadi-Eydivand, M., and Fathi-Roudsari, M. "Amine-functionalized single-walled carbon nanotube/polycaprolactone electrospun scaffold for bone tissue engineering: *in vitro* study." *Fibers and Polymers* **20**(9):pp. 1869–1882, pp. 1869–1882

[5] Gaharwar, A. K. et al. "Nanoclay-enriched poly (ε-caprolactone) electrospun scaffolds for osteogenic differentiation of human mesenchymal stem cells." *Tissue Engineering Part A* **20**(15-16):pp. 2088–2101, pp. 2088–2101

[6] Papageorgiou, D. G., Roumeli, E., Terzopoulou, Z., Tsanaktsis, V., Chrissafis, K., and Bikiaris, D. "Polycaprolactone/multi-wall carbon nanotube nanocomposites prepared by in situ ring opening polymerization: Decomposition profiling using thermogravimetric analysis and analytical pyrolysis-gas chromatography/mass spectrometry." *Journal of Analytical and Applied Pyrolysis* **115**:pp. 125–131, pp. 125–131

[7] Omidvar, N., Ganji, F., and Eslaminejad, M. B. "*In vitro* osteogenic induction of human marrow-derived mesenchymal stem cells by PCL fibrous scaffolds containing dexamethazone-loaded chitosan microspheres." *Journal of biomedical materials research Part A* **104**(7):pp. 1657–1667, pp. 1657–1667

[8] Khodabandeh, A., Yousefi, A. A., Jafarzadeh-Holagh, S., and Vasheghani-Farahani, E. "Fabrication of 3D microfibrous composite polycaprolactone/hydroxyapatite scaffolds loaded with piezoelectric poly (lactic acid) nanofibers by sequential near-field and conventional electrospinning for bone tissue engineering." *Biomaterials Advances* **166**:p. 214053, p. 214053

[9] Grenier, J., Duval, H., Barou, F., Lv, P., David, B., and Letourneur, D. "Mechanisms of pore formation in hydrogel scaffolds textured by freeze-drying." *Acta Biomaterialia* **94**:pp. 195–203, pp. 195–203

[10] Zhang, H. et al. "Enhanced compressive strength and *in vitro* degradation of porous pectin/calcium phosphate cement scaffolds by freeze casting without sintered." *Journal of Materials Research and Technology* **34**:pp. 125–135, pp. 125–135

[11] Suhaimin, I. S., Kassim, S. A., Zubir, S. A., and Abdullah, T. K. "Effect of bioactive glass on the properties of glass/polymer composite scaffold fabricated by solvent casting/particulate leaching technique." *Journal of Thermoplastic Composite Materials*:p. 08927057251314420, p. 08927057251314420

[12] Song, Y. "Liquid–liquid phase separation-inspired design of biomaterials." *Biomaterials Science* **12**(8):pp. 1943–1949, pp. 1943–1949

[13] Shahrubudin, N., Lee, T. C., and Ramlan, R. "An overview on 3D printing technology: Technological, materials, and applications." *Procedia manufacturing* **35**:pp. 1286–1296, pp. 1286–1296

[14] Ghosal, K. et al. "Electrospinning over solvent casting: tuning of mechanical properties of membranes." *Scientific reports* **8**(1):pp. 1–9, pp. 1–9

[15] U. D'Amora, M. et al. "Collagen density gradient on three-dimensional printed poly (ε-caprolactone) scaffolds for interface tissue engineering." *Journal of tissue engineering and regenerative medicine* **12**(2):pp. 321–329, pp. 321–329

[16] Woodruff, M. A. and Hutmacher, D. W. "The return of a forgotten polymer-Polycaprolactone in the 21st century." *Progress in polymer science* **35**(10):pp. 1217–1256, pp. 1217–1256

[17] Ghorbani, F. M., Kaffashi, B., Shokrollahi, P., Seyedjafari, E., and Ardeshirylajimi, A. "PCL/chitosan/Zn-doped nHA electrospun nanocomposite scaffold promotes adipose derived stem cells adhesion and proliferation." *Carbohydrate polymers* **118**:pp. 133–142, pp. 133–142

[18] Gomes, S. R. et al. "*In vitro* and *in vivo* evaluation of electrospun nanofibers of PCL, chitosan and gelatin: A comparative study." *Materials Science and Engineering: C* **46**:pp. 348–358, pp. 348–358

[19] Semnani, D. et al. "Evaluation of PCL/chitosan electrospun nanofibers for liver tissue engineering." *International Journal of Polymeric Materials and Polymeric Biomaterials* **66**(3):pp. 149–157, pp. 149–157

[20] Jayakumar, R., Prabaharan, M., Nair, S., and Tamura, H. "Novel chitin and chitosan nanofibers in biomedical applications." *Biotechnology advances* **28**(1):pp. 142–150, pp. 142–150

[21] Su, W.-T., Wang, Y.-T., and Chou, C.-M. "Optimal fluid flow enhanced mineralization of MG-63 cells in porous chitosan scaffold." *Journal of the Taiwan Institute of Chemical Engineers* **45**(4):pp. 1111–1118, pp. 1111–1118

[22] Hsu, Y.-K. et al. "The effect of adipose-derived mesenchymal stem cells and chondrocytes with platelet-rich fibrin releasates augmentation by intra-articular injection on acute osteochondral defects in a rabbit model." *The Knee* **25**(6):pp. 1181–1191, pp. 1181–1191

[23] Gassling, V., Hedderich, J., Açil, Y., Purcz, N., Wiltfang, J., and Douglas, T. "Comparison of platelet rich fibrin and collagen as osteoblast-seeded scaffolds for bone tissue engineering applications." *Clinical Oral Implants Research* **24**(3):pp. 320–328, pp. 320–328

[24] Eom, Y. W. et al. "The role of growth factors in maintenance of stemness in bone marrow-derived mesenchymal stem cells." *Biochemical and biophysical research communications* **445**(1):pp. 16–22, pp. 16–22

[25] Jee, Y.-J. "Use of platelet-rich fibrin and natural bone regeneration in regenerative surgery." *Journal of the Korean Association of Oral and Maxillofacial Surgeons* **45**(3):p. 121, p. 121

[26] Ye, H., Zhu, J., Deng, D., Jin, S., Li, J., and Man, Y. "Enhanced osteogenesis and angiogenesis by PCL/chitosan/Sr-doped calcium phosphate electrospun nanocomposite membrane for guided bone regeneration, Journal of Biomaterials Science." *Polymer Edition* **30**(16):pp. 1505–1522, pp. 1505–1522

[27] Surucu, S. and Sasmazel, H. T. "Development of core-shell coaxially electrospun composite PCL/chitosan scaffolds." *International journal of biological macromolecules* **92**:pp. 321–328, pp. 321–328

[28] Shimojo, A., Perez, A., Galdames, S., Brissac, I., and Santana, M. "Stabilization of porous chitosan improves the performance of its association with platelet-rich plasma as a composite scaffold." *Materials Science and Engineering: C* **60**:pp. 538–546, pp. 538–546

[29] Chi, H. et al. "Chitosan-Gelatin Scaffolds Incorporating Decellularized Platelet-Rich Fibrin Promote Bone Regeneration." *ACS Biomaterials Science & Engineering* **5**(10):pp. 5305–5315, pp. 5305–5315

[30] Ansarizadeh, M., Mashayekhan, S., and Saadatmand, M. "Fabrication, modeling and optimization of lyophilized advanced platelet rich fibrin in combination with collagen-chitosan as a guided bone regeneration membrane." *International journal of biological macromolecules* **125**:pp. 383–391, pp. 383–391

[31] Choukroun, J., Adda, F., Schoeffler, C., and Vervelle, A. "Une opportunité en paro-implantologie: le PRF." *Implantodontie* **42**(55):e62, e62

[32] Edwards, A., Jarvis, D., Hopkins, T., Pixley, S., and Bhattarai, N. "Poly (ε-caprolactone)/keratin-based composite nanofibers for biomedical applications." *Journal of Biomedical Materials Research Part B: Applied Biomaterials* **103**(1):pp. 21–30, pp. 21–30

[33] Rafiei, M., Jooybar, E., Abdekhodaie, M. J., and Alvi, M. "Construction of 3D fibrous PCL scaffolds by coaxial electrospinning for protein delivery." *Materials Science and Engineering: C* **113**:p. 110913, p. 110913

[34] Gryshkov, O. et al. "Porous biomorphic silicon carbide ceramics coated with hydroxyapatite as prospective materials for bone implants." *Materials Science and Engineering: C* **68**:pp. 143–152, pp. 143–152

[35] Rabanel, J.-M., Faivre, J., Paka, G. D., Ramassamy, C., Hildgen, P., and Banquy, X. "Effect of polymer architecture on curcumin encapsulation and release from PEGylated polymer nanoparticles: Toward a drug delivery nano-platform to the CNS." *European Journal of Pharmaceutics and Biopharmaceutics* **96**:pp. 409–420, pp. 409–420

[36] Mahmoodi, M., Khosroshahi, M., and Atyabi, F. "EARLY EXPERIMENTAL RESULTS OF THROMBOLYSIS USING CONTROLLED RELEASE OF TISSUE PLASMINOGEN ACTIVATOR ENCAPSULATED BY PLGA/CS NANOPARTICLES DELIVERED BY PULSE 532 nm LASER." *Digest Journal of Nanomaterials & Biostructures (DJNB)* **6**(4)

[37] Ahmaditabar, P., Mahmoodi, M., Taheri, R. A., and Asefnejad, A. "Laser thrombolysis and *in vitro* release kinetics of tPA encapsulated in chitosan polysulfate-coated nanoliposome." *Carbohydrate Polymers* **299**:p. 120225, p. 120225

[38] Kokubo, T. and Takadama, H. "How useful is SBF in predicting in vivo bone bioactivity?" *Biomaterials* **27**(15):pp. 2907–2915, pp. 2907–2915

[39] Shao, W. et al. "Enhanced bone formation in electrospun poly (l-lactic-co-glycolic acid)-tussah silk fibroin ultrafine nanofiber scaffolds incorporated with graphene oxide." *Materials Science and Engineering: C* **62**:pp. 823–834, pp. 823–834

[40] Wang, Q. et al. "A graded graphene oxide-hydroxyapatite/silk fibroin biomimetic scaffold for bone tissue engineering." *Materials Science and Engineering: C* **80**:pp. 232–242, pp. 232–242

[41] Surucu, S., Masur, K., Sasmazel, H. T., T. Von, W., and Weltmann, K. D. "Atmospheric plasma surface modifications of electrospun PCL/chitosan/PCL hybrid scaffolds by nozzle type plasma jets for usage of cell cultivation." *Applied Surface Science* **385**:pp. 400–409, pp. 400–409

[42] Roozbahani, F., Sultana, N., A. Fauzi, I., and Nouparvar, H. "Effects of chitosan alkali pretreatment on the preparation of electrospun PCL/chitosan blend nanofibrous scaffolds for tissue engineering application." *Journal of Nanomaterials* **2013**

[43] Fridrikh, S. V., Jian, H. Y., Brenner, M. P., and Rutledge, G. C. "Controlling the fiber diameter during electrospinning." *Physical review letters* **90**(14):p. 144502, p. 144502

[44] Chen, H.-W. and Lin, M.-F. "Characterization, Biocompatibility, and Optimization of Electrospun SF/PCL/CS Composite Nanofibers." *Polymers* **12**(7):p. 1439, p. 1439

[45] D. M. dos, S., Chagas, P. A., Leite, I. S., Inada, N. M., et al. "Core-sheath nanostructured chitosan-based nonwovens as a potential drug delivery system for periodontitis treatment." *International journal of biological macromolecules* **142**:pp. 521–534, pp. 521–534

[46] Sedghi, R., Gholami, M., Shaabani, A., Saber, M., and Niknejad, H. "Preparation of novel chitosan derivative nanofibers for prevention of breast cancer recurrence." *European Polymer Journal* **123**:p. 109421, p. 109421

[47] Liu, J. et al. "Bonding performance of melamine-urea-formaldehyde and phenol-resorcinol-formaldehyde adhesive glulams at elevated temperatures." *International Journal of Adhesion and Adhesives* **98**:p. 102500, p. 102500

[48] Krainer, S. and Hirn, U. "Contact angle measurement on porous substrates: Effect of liquid absorption and drop size." *Colloids and Surfaces A: Physicochemical and Engineering Aspects* **619**:p. 126503, p. 126503

[49] Erbil, H. Y. "The debate on the dependence of apparent contact angles on drop contact area or three-phase contact line: A review." *Surface Science Reports* **69**(4):pp. 325–365, pp. 325–365

[50] Mirjalili, F. and Mahmoodi, M. "Controlled release of protein from gelatin/chitosan hydrogel containing platelet-rich fibrin encapsulated in chitosan nanoparticles for accelerated wound healing in an animal model." *International Journal of Biological Macromolecules* **225**:pp. 588–604, pp. 588–604

[51] Kim, M. and Kim, G. "Electrospun PCL/phlorotannin nanofibres for tissue engineering: Physical properties and cellular activities." *Carbohydrate polymers* **90**(1):pp. 592–601, pp. 592–601

[52] Mitropoulou, A., Markatos, D. N., Dimopoulos, A., Marazioti, A., Mikelis, C.-M., and Mavrilas, D. "Development and evaluation of biodegradable core-shell microfibrous and nanofibrous scaffolds for tissue engineering applications." *Journal of Materials Science: Materials in Medicine* **35**(1):p. 10, p. 10

[53] Melnik, E. V., Shkarina, S. N., Ivlev, S. I., Weinhardt, V., et al. "*In vitro* degradation behaviour of hybrid electrospun scaffolds of polycaprolactone and strontium-containing hydroxyapatite microparticles." *Polymer Degradation and Stability* **167**:pp. 21–32, pp. 21–32

[54] Mndlovu, H., Kumar, P., L. C. du, T., and Choonara, Y. E. "A review of bio material degradation assessment approaches employed in the biomedical field." *NPJ Materials Degradation* **8**(1):p. 66, p. 66

[55] Baker, B. M., Trappmann, B., Wang, W. Y., Sakar, M. S., et al. "Cell-mediated fibre recruitment drives extracellular matrix mechanosensing in engineered fibrillar microenvironments." *Nature materials* **14**(12):pp. 1262–1268, pp. 1262–1268

[56] Fadaie, M., Mirzaei, E., Geramizadeh, B., and Asvar, Z. "Incorporation of nanofibrillated chitosan into electrospun PCL nanofibers makes scaffolds with enhanced mechanical and biological properties." *Carbohydrate polymers* **199**:pp. 628–640, pp. 628–640

[57] Bölgen, N., Menceloğlu, Y. Z., Acatay, K., Vargel, I., and Pişkin, E. "*In vitro* and *in vivo* degradation of non-woven materials made of poly (ε-caprolactone) nanofibers prepared by electrospinning under different conditions." *Journal of Biomaterials Science, Polymer Edition* **16**(12):pp. 1537–1555, pp. 1537–1555

[58] Asvar, Z., Mirzaei, E., Azarpira, N., Geramizadeh, B., and Fadaie, M. "Evaluation of electrospinning parameters on the tensile strength and suture retention strength of polycaprolactone nanofibrous scaffolds through surface response methodology." *Journal of the mechanical behavior of biomedical materials* **75**:pp. 369–378, pp. 369–378

[59] Kwon, I. K., Kidoaki, S., and Matsuda, T. "Electrospun nano-to microfiber fabrics made of biodegradable copolyesters: structural characteristics mechanical properties and cell adhesion potential." *Biomaterials* **26**(18):pp. 3929–3939, pp. 3929–3939

[60] Mahoney, C., Conklin, D., Waterman, J., Sankar, J., and Bhattarai, N. "Electrospun nanofibers of poly (ε-caprolactone)/depolymerized chitosan for respiratory tissue engineering applications." *Journal of Biomaterials science, Polymer edition* **27**(7):pp. 611–625, pp. 611–625

[61] Rambhia, K. J. and Ma, P. X. "Controlled drug release for tissue engineering." *Journal of Controlled Release* **219**:pp. 119–128, pp. 119–128

[62] Abazari, M. F. et al. "Platelet-rich plasma incorporated electrospun PVA-chitosan-HA nanofibers accelerates osteogenic differentiation and bone reconstruction." *Gene* **720**:p. 144096, p. 144096

[63] Jain, E., Chinzei, N., Blanco, A., Case, N., et al. "Platelet-rich plasma released from polyethylene glycol hydrogels exerts beneficial effects on human chondrocytes." *Journal of Orthopaedic Research* **37**(11):pp. 2401–2410, pp. 2401–2410

[64] Mircioiu, C., Voicu, V., Anuta, V., Tudose, A., Celia, C., et al. "Mathematical modeling of release kinetics from supramolecular drug delivery systems." *Pharmaceutics* **11**(3):p. 140, p. 140

[65] Abdullahi, I. and Zainol, I. "Synthesis, Characterization and Bioactivity of Chitosan Hydroxyapatite Composite Doped with Strontium." *Solid State Phenomena* **317**:pp. 217–226, pp. 217–226

[66] Pathmanapan, S., Periyathambi, P., and Anandasadagopan, S. K. "Fibrin hydrogel incorporated with graphene oxide functionalized nanocomposite scaffolds for bone repair-*In vitro* and *in vivo* study." *Nanomedicine: Nanotechnology, Biology and Medicine* **29**:p. 102251, p. 102251

[67] C. del, R., Rodríguez-Évora, M., et al. "BMP-2, PDGF-BB, and bone marrow mesenchymal cells in a macroporous β-TCP scaffold for critical-size bone defect repair in rats." *Biomedical materials* **10**(4):p. 045008, p. 045008

[68] Cheng, G., Ma, X., Li, J., Cheng, Y., Cao, Y., et al. "Incorporating platelet-rich plasma into coaxial electrospun nanofibers for bone tissue engineering." *International journal of pharmaceutics* **547**(1-2):pp. 656–666, pp. 656–666

[69] Christopherson, G. T., Song, H., and Mao, H.-Q. "The influence of fiber diameter of electrospun substrates on neural stem cell differentiation and proliferation." *Biomaterials* **30**(4):pp. 556–564, pp. 556–564

[70] Webster, T. J., Schadler, L. S., Siegel, R. W., and Bizios, R. "Mechanisms of enhanced osteoblast adhesion on nanophase alumina involve vitronectin." *Tissue engineering* **7**(3):pp. 291–301, pp. 291–301

[71] Qian, Y., Zhang, Z., Zheng, L., Song, R., and Zhao, Y. "Fabrication and characterization of electrospun polycaprolactone blended with chitosan-gelatin complex nanofibrous mats." *Journal of Nanomaterials* **2014**

[72] Song, Y., Lin, K., He, S., Wang, C., et al. "Nano-biphasic calcium phosphate/polyvinyl alcohol composites with enhanced bioactivity for bone repair via low-temperature three-dimensional printing and loading with platelet-rich fibrin." *International journal of nanomedicine*:pp. 505–523, pp. 505–523

[73] Qi, R., Cao, X., Shen, M., Guo, R., Yu, J., and Shi, X. "Biocompatibility of electrospun halloysite nanotube-doped poly (lactic-co-glycolic acid) composite nanofibers." *Journal of Biomaterials Science, Polymer Edition* **23**(1-4):pp. 299–313, pp. 299–313

[74] Norouz, F., Halabian, R., Salimi, A., and Ghollasi, M. "A new nanocomposite scaffold based on polyurethane and clay nanoplates for osteogenic differentiation of human mesenchymal stem cells *in vitro*." *Materials Science and Engineering: C* **103**:p. 109857, p. 109857

[75] De-Paula, M. M. M., Afewerki, S., Viana, B. C., Webster, T. J., Lobo, A. O., and Marciano, F. R. "Dual effective core-shell electrospun scaffolds: Promoting osteoblast maturation and reducing bacteria activity." *Materials Science and Engineering: C* **103**:p. 109778, p. 109778

[76] Choukroun, J., Diss, A., Simonpieri, A., Girard, M.-O., Schoeffler, C., et al. "Platelet-rich fibrin (PRF): a second-generation platelet concentrate. Part IV: clinical effects on tissue healing." *Oral Surgery, Oral Medicine, Oral Pathology, Oral Radiology, and Endodontology* **101**(3):e56–e60, e56–e60

[77] Kim, J.-S., Jeong, M.-H., Jo, J.-H., Kim, S.-G., and Oh, J.-S. "Clinical application of platelet-rich fibrin by the application of the double J technique during implant placement in alveolar bone defect areas." *Implant dentistry* **22**(3):pp. 244–249, pp. 244–249

[78] Wu, M., Chen, G., and Li, Y.-P. "TGF-β and BMP signaling in osteoblast, skeletal development, and bone formation, homeostasis and disease." *Bone research* **4**:p. 16009, p. 16009

[79] Utomo, D. N., Mahyudin, F., Hernugrahanto, K. D., Suroto, H., Chilmi, M. Z., and Rantam, F. A. "Implantation of platelet rich fibrin and allogenic mesenchymal stem cells facilitate the healing of muscle injury: An experimental study on animal." *International Journal of Surgery Open* **11**:pp. 4–9, pp. 4–9

[80] Lukášováá, V., Buzgo, M., Vocetková, K., et al. "Needleless electrospun and centrifugal spun poly-ε-caprolactone scaffolds as a carrier for platelets in tissue engineering applications: A comparative study with hMSCs." *Materials Science and Engineering: C* **97**:pp. 567–575, pp. 567–575

[81] Gregory, C. A., Gunn, W. G., Peister, A., and Prockop, D. J. "An Alizarin red-based assay of mineralization by adherent cells in culture: comparison with cetylpyridinium chloride extraction." *Analytical biochemistry* **329**(1):pp. 77–84, pp. 77–84

[82] Wang, Z. et al. "Osteoblastic mesenchymal stem cell sheet combined with C houkroun platelet-rich fibrin induces bone formation at an ectopic site." *Journal of Biomedical Materials Research Part B: Applied Biomaterials* **103**(6):pp. 1204–1216, pp. 1204–1216

[83] Blinder, Y., Mooney, D., and Levenberg, S. "Engineering approaches for inducing blood vessel formation." *Current opinion in chemical engineering* **3**:pp. 56–61, pp. 56–61

[84] Shi, X., Zhou, K., Huang, F., and Wang, C. "Interaction of hydroxyapatite nanoparticles with endothelial cells: internalization and inhibition of angiogenesis *in vitro* through the PI3K/Akt pathway." *International journal of nanomedicine*:pp. 5781–5795, pp. 5781–5795

[85] Feng, C., Xue, J., Yu, X., Zhai, D., Lin, R., et al. "Co-inspired hydroxyapatite-based scaffolds for vascularized bone regeneration." *Acta Biomaterialia* **119**:pp. 419–431, pp. 419–431

[86] Pezzatini, S. et al. "Nanostructured HA crystals up-regulate FGF-2 expression and activity in microvascular endothelium promoting angiogenesis." *Bone* **41**(4):pp. 523–534, pp. 523–534

[87] Lai, H.-J., Kuan, C.-H., Wu, H.-C., Tsai, J.-C., et al. "Tailored design of electrospun composite nanofibers with staged release of multiple angiogenic growth factors for chronic wound healing." *Acta biomaterialia* **10**(10):pp. 4156–4166, pp. 4156–4166

[88] Xie, Z., Paras, C. B., Weng, H., Punnakitikashem, P., et al. "Dual growth factor releasing multi-functional nanofibers for wound healing." *Acta biomaterialia* **9**(12):pp. 9351–9359, pp. 9351–9359